NEUROSCIENCE

VMAT2 dysfunction impairs vesicular dopamine uptake, driving its oxidation and α-synuclein pathology in DJ-1–linked Parkinson's neurons

Leonie M. Heger[1,2], Francesco Gubinelli[1], Andreas J. Huber[1,2], Aida Cardona-Alberich[1], Matteo Rovere[1,2], Ulf Matti[3], Stephan A. Müller[4,5], Sankarshana R. Nagaraja[6,7], Lena Jaschkowitz[1], Martina Schifferer[5,6], Wolfgang Wurst[5,6,8], Stefan F. Lichtenthaler[4,5,6], Christian Behrends[6,7], Sivakumar Sambandan[9,10], Lena F. Burbulla[1,5,6]*

Parkinson's disease (PD) is characterized by α-synuclein accumulation and dopaminergic neuron degeneration, with dopamine (DA) oxidation emerging as a key pathological driver. However, the mechanisms underlying this neurotoxic process remain unclear. Using PD patient-derived and CRISPR-engineered induced pluripotent stem cell midbrain dopaminergic neurons lacking DJ-1, we identified defective sequestration of cytosolic DA into synaptic vesicles, which culminated in DA oxidation and α-synuclein pathology. In-depth proteomics, state-of-the-art imaging, and ultrasensitive DA probes uncovered that decreased vesicular monoamine transporter 2 (VMAT2) protein and function impaired vesicular DA uptake, resulting in reduced vesicle availability and abnormal vesicle morphology. Furthermore, VMAT2 activity and vesicle endocytosis are processes dependent on adenosine 5′-triphosphate (ATP), which is notably reduced in DJ-1–deficient dopaminergic neurons. ATP supplementation restored vesicular function and alleviated DA-related pathologies in mutant dopaminergic neurons. This study reveals an ATP-sensitive mechanism that regulates DA homeostasis through VMAT2 and vesicle dynamics in midbrain dopaminergic neurons, highlighting enhanced DA sequestration as a promising therapeutic strategy for PD.

INTRODUCTION

Understanding the pathophysiology of neurodegenerative diseases is crucial for identifying therapeutic targets and developing effective treatments. Parkinson's disease (PD), the second most common neurodegenerative disorder, affects ~1% of individuals over 65 years of age and 4% of those over 85 years of age. While most cases are sporadic, 5 to 10% are attributed to inherited cases (*1*). PD is marked by the pathological accumulation of α-synuclein into Lewy bodies and the progressive loss of dopaminergic neurons in the substantia nigra (SN), leading to characteristic motor symptoms such as tremor and rigidity (*2*). Current treatments offer only symptomatic relief without slowing neuronal degeneration. Our understanding of the pathways underlying the differential vulnerability of SN dopaminergic neurons in PD remains limited. Uncovering the mechanisms behind the depletion of this specific neuron subpopulation and understanding the progression of disease in more detail are crucial for the development of disease-modifying therapies.

A time-dependent pathological cascade has been recently uncovered, starting with mitochondrial dysfunction and leading to dopamine (DA) oxidation and α-synuclein accumulation in DJ-1 (*PARK7*)–linked PD as well as in other genetic and sporadic forms of PD (*3*). Notably, this pathogenic cascade was not recapitulated in PD mouse models, and species-specific differences in DA metabolism are likely to contribute to this discrepancy. In particular, PD mouse models lacked the accumulation of oxidized DA characteristic of human midbrain neurons (*3*). This fundamental difference suggests that as-yet-unknown mechanisms prevent the formation of oxidized DA in mice. This may, at least in part, explain the relative resistance of rodent neurons to degeneration in genetic models of PD while also underscoring the critical role of DA oxidation in the vulnerability of human SN neurons to PD-linked mutations.

In general, the oxidation of DA is dependent on various factors, beginning with an excess of cytosolic DA that is not properly sequestered into synaptic vesicles (*4*). If, for various reasons, this pathway fails or is reaching its capacity, DA is enzymatically degraded through specific enzymes (*5*). This sensitive regulation is particularly important as the accumulation of cytosolic DA generates reactive oxygen species and DA quinones (*6*, *7*), derivates of oxidized DA, that can form toxic adducts with proteins (*3*, *8*, *9*) and may lead to neuron damage and death (*10*). This pathway lastly results in the formation of neuromelanin (NM), a polymer pigment concentrated in human—but not mouse—SN midbrain dopaminergic neurons (*11*). NM is thought to play a protective role by preventing toxic DA accumulation and scavenging metals (*12*). However, while altered mitochondrial function was suggested to contribute to oxidized DA formation and broader PD pathogenesis, the mechanisms by which mitochondrial dysfunction leads to excess cytosolic DA, triggering its oxidation, and whether targeting mitochondrial health would work as a therapeutic approach to counteract oxidized DA are largely unexplored. Dopaminergic neurons are particularly vulnerable to oxidative stress because of their autonomous pacemaking activity and extensive axonal arborization, both of which contribute to elevated mitochondrial oxidant stress (*13*).

---

[1] Metabolic Biochemistry, Biomedical Center (BMC), Faculty of Medicine, LMU Munich, Munich, Germany. [2] Graduate School of Systemic Neurosciences (GSN), LMU Munich, Munich, Germany. [3] Abberior Instruments GmbH, Göttingen, Germany. [4] Neuroproteomics, School of Medicine and Health, TUM University Hospital, Technical University of Munich, Germany. [5] German Center for Neurodegenerative Diseases (DZNE), Munich, Germany. [6] Munich Cluster for Systems Neurology (SyNergy), Munich, Germany. [7] Faculty of Medicine, LMU Munich, Munich, Germany. [8] Helmholtz Munich, Institute of Developmental Genetics, Technical University Munich, Institute of Developmental Genetics, Munich, Germany. [9] Laboratory of Neurobiology, Max Planck Institute for Multidisciplinary Sciences, Göttingen, Germany. [10] Synaptic Metal Ion Dynamics and Signaling, Max Planck Institute for Multidisciplinary Sciences, Göttingen, Germany.
*Corresponding author. Email: lena.burbulla@med.uni-muenchen.de

It has been well established that DA signaling and metabolism are largely regulated by the synergistic interplay of tyrosine hydroxylase (TH), vesicular monoamine transporter 2 (VMAT2), and DA transporter (DAT). While TH catalyzes the conversion of tyrosine to L-DOPA (L-3,4-dihydroxyphenylalanine), which is subsequently converted to DA by DOPA decarboxylase, VMAT2 and DAT are specific membrane transporters responsible for transporting DA from the cytosol into synaptic vesicles and across the plasma membrane back into the cytosol of the presynaptic neuron, respectively. In particular, VMAT2 requires a proton electrochemical gradient generated in the synaptic vesicle lumen by vacuolar adenosine triphosphatase (ATPase), which, in turn, depends on adenosine 5′-triphosphate (ATP) primarily sourced from local mitochondria, to package DA (*14*) from the cytosol into synaptic vesicles (*15*, *16*). Therefore, VMAT2 relies on a well-working mitochondrial function for sufficient ATP delivery. By regulating the concentration or number of DA neurotransmitter molecules sequestered per vesicle, i.e., the quantal size, VMAT2 also largely determines the quantity of DA release into the synaptic cleft (*15*). A study has indicated a reduction in VMAT2 activity and DA uptake in isolated DA storage vesicles from striatal PD brain tissue (*17*). VMAT2 dysfunction is therefore one potential source for toxic DA products because of increased unsequestered cytosolic DA. However, why VMAT2 activity is reduced in PD brain tissue—and whether targeting VMAT2 deficiency or improving its function could be beneficial in human disease models or even therapeutically—remains poorly investigated, particularly in disease-relevant human model systems.

Notably, DJ-1 has been previously identified to directly interact with VMAT2 within a human neuroblastoma cell line, and pathogenic DJ-1 mutants lacked the ability to stimulate VMAT2 activity, suggesting a direct mechanistic link between DJ-1 function and vesicular DA storage (*18*). Given that DJ-1 deficiency leads to mitochondrial dysfunction and reduced ATP levels, and functional VMAT2 relies on sufficient ATP supply, elaborating this DJ-1-VMAT2 axis could be a promising strategy for mitigating dopaminergic toxicity in PD.

Despite the central role of DA handling in PD, relatively little is known about VMAT2 dysfunction and synaptic vesicle abnormalities and their link to mitochondrial function in both genetic and sporadic forms of the disease. This knowledge gap is particularly evident in disease-relevant human models, where synaptic dysfunction remains poorly characterized.

In this study, we aimed at investigating underlying mechanisms of dopaminergic neuron vulnerability linked to factors leading to oxidized DA accumulation. Using induced pluripotent stem cell (iPSC)–derived midbrain dopaminergic neurons from a patient with DJ-1–linked PD and two *DJ-1* knockout (KO) lines, our results strongly link the loss of this redox-sensitive protein with a reduction in VMAT2 abundance across multiple magnitudes of spatial dimensions. In addition to this, VMAT2 transporter activity was diminished because of lowered ATP levels in DJ-1–deficient neurons. These combined pathologies resulted in a reduced uptake of DA into synaptic vesicles, leading to oxidized DA and α-synuclein pathology in mutant neurons. Unbiased and targeted proteomic analyses strengthened the link of DJ-1 with intracellular vesicles and synaptic components, an association that is heavily diminished in DJ-1–deficient neurons. Last, we show that targeting ATP depletion in these PD-linked neurons partially alleviates the observed PD-associated pathologies, offering a potential approach benefiting neuronal survival. Our study provides insights into whether and how the main route of DA sequestration through VMAT2-mediated uptake into synaptic vesicles is altered in PD-linked neurons, a potential underlying mechanism for DA oxidation and vulnerability of SN midbrain neurons.

RESULTS

Proteomic analysis reveals the deficiency of VMAT2 and down-regulation of pathways associated with synaptic vesicles in DJ-1–deficient dopaminergic neurons

Oxidized DA accumulation has been described in DJ-1–deficient iPSC-derived midbrain dopaminergic neurons (*3*); however, the source of this potentially neurotoxic insult affecting neuron vulnerability remains elusive. To uncover underlying pathways of the observed DA oxidation, we differentiated iPSCs from two *DJ-1* KO lines (*DJ-1* KO #1 and #2 = DJ-1^{KOs}) generated by gene editing using CRISPR-Cas9 and their respective healthy control counterparts (CTRL #1 and #2 = CTRLs) (*3*) into midbrain dopaminergic neurons (figs. S1 and S2).

In detail, iPSCs expressed key pluripotency markers (SSEA4, OCT4, NANOG, and SOX2) as confirmed by immunocytochemistry (fig. S1, A and B). Quantitative polymerase chain reaction (qPCR) analysis showed strong up-regulation of pluripotency-related genes compared to human fibroblasts (fig. S1C). Spontaneous differentiation demonstrated the capacity of all lines to generate cells from all three germ layers (ectoderm, mesoderm, and endoderm), as shown by qPCR (fig. S1D). Quality control of dopaminergic neurons at days 30 and 70 of differentiation (fig. S2, A and B) revealed homogeneous, sustained expression of dopaminergic and neuronal markers, indicating successful induction and maturation. Western blot analysis confirmed the expression of TH and β-III-tubulin and validated the loss of DJ-1 in DJ-1–deficient lines (fig. S2C).

Using these two pairs of CRISPR-edited *DJ-1* KO neuronal lines with their respective isogenic counterparts, we performed unbiased mass spectrometry (MS)–based proteomics. Here, we identified two distinct sets of proteins that are up-regulated (385 proteins) and down-regulated (104 proteins) in neurons from both *DJ-1* KO lines [P value <0.05 and $\log_2$ fold change (FC) larger than 0.5 or smaller than −0.5] compared to controls (Fig. 1A and table S1). Notably, the DA vesicle transporter VMAT2 was found among the top three down-regulated proteins in *DJ-1* KO neurons, following PARK7 (DJ-1) as the most down-regulated and PCDAC [also known as PCDHA12 (protocadherin alpha-12)], a protocadherin family member functioning as a calcium-dependent cell-adhesion molecule, as the second. Other proteins found to be differentially regulated in *DJ-1* KO neurons further indicated alterations in synaptic function in association with neuronal signaling, such as the decreased abundance of PTPRT (protein tyrosine phosphatase receptor type T), identified as a risk factor common to sporadic PD (*19*, *20*), and AT2A3 [also known as SERCA3 (sarco/endoplasmic reticulum Ca^{2+}-ATPase 3)] (*21*).

In addition, we performed Gene Ontology (GO) enrichment analysis for the cellular component (Fig. 1B), molecular function (fig. S3A), and biological process (fig. S4A) of the differentially expressed proteins. We ranked the top 10 GO terms for either up- or down-regulated proteins by significance and, among others, found a prominent enrichment of down-regulated proteins for the terms "synapse" and "synaptic vesicle" associated with the cellular compartment (Fig. 1B), "transmembrane transporter binding" and "calcium ion binding" associated with the molecular function (fig. S3A),

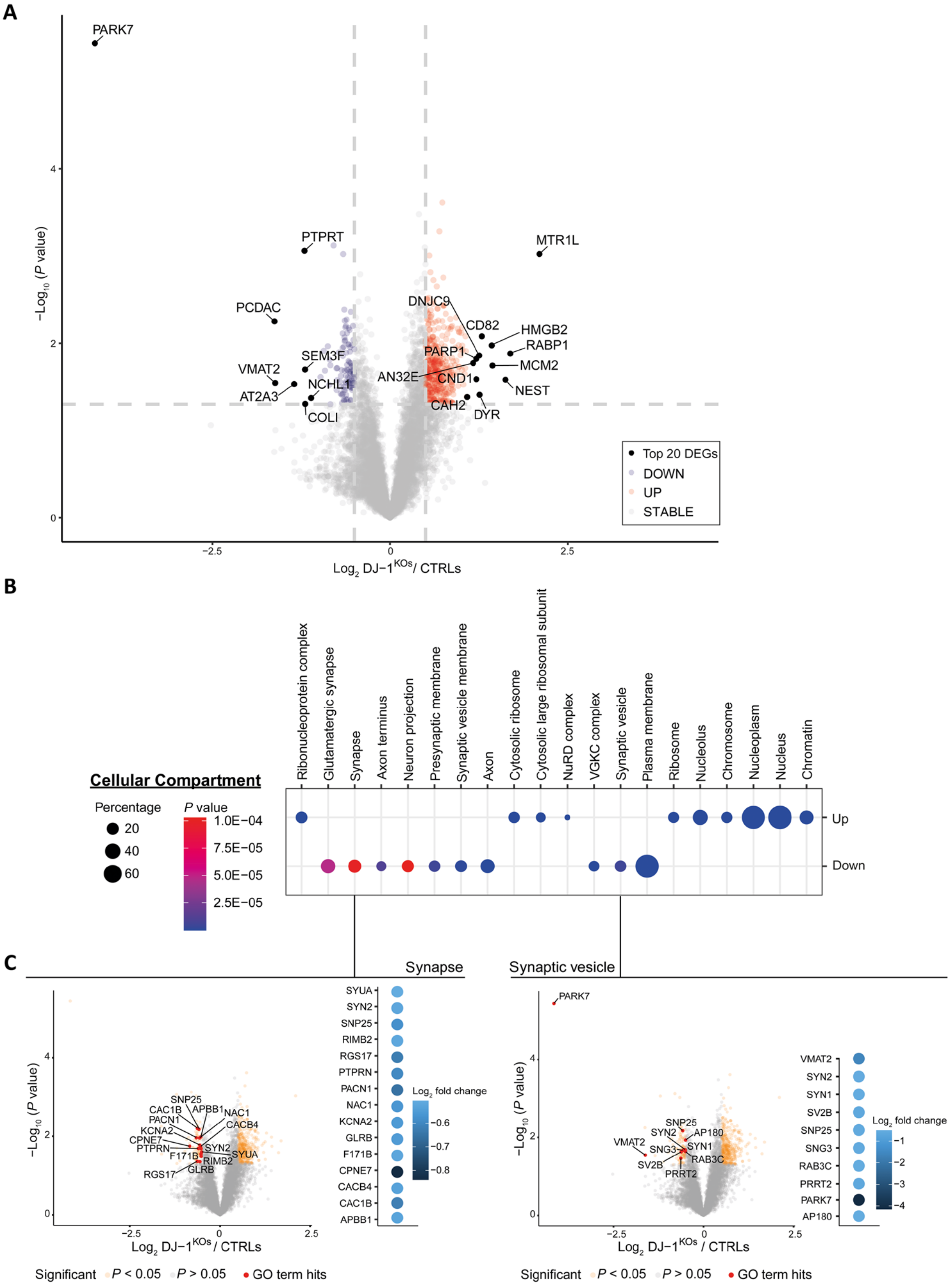

Fig. 1. Whole-cell proteomic analysis of DJ-1–deficient dopaminergic neurons. (**A**) Volcano plots of *DJ-1* KO (both lines) versus isogenic control (both lines) dopaminergic neurons. The $-\log_{10}$-transformed *P* values of each protein are plotted against their $\log_2$ fold change–transformed protein label-free quantification ratios. Proteins significantly more abundant in the proteome of *DJ-1* KO neurons are displayed as red-filled dots, while less abundant proteins are displayed as blue-filled dots. Unaltered proteins are displayed as gray dots. Top 20 differentially expressed proteins are labeled with their UniProt gene names ($n = 4$). (**B**) Results of GO enrichment analysis for cellular component (GOTERM_CC_DIRECT) using the web tool DAVID (version 6.8). Differentially expressed proteins (*P* value <0.05 and $\log_2$ fold change >0.5 or <−0.5) were compared to the background of all proteins detected under both conditions. The dot plots show the total gene number of a term in percentage as a dot size and the *P* values as a color gradient. The top 10 terms for either enriched (Up) or down-regulated (Down) proteins are presented. (**C**) Volcano and dot plots of the differentially expressed proteins in *DJ-1* KO neurons involved in the terms "synapse" (left) and "synaptic vesicle" (right) associated with the cellular compartment.

and "chemical synaptic transmission" associated with the biological process (fig. S4A) in *DJ-1* KO neurons.

We performed a more in-depth analysis of the above outlined down-regulated pathways and visualized the respective differentially expressed proteins of these pathways via volcano plots and dot plots (Fig. 1C and figs. S3B and S4B). VMAT2 prominently presented with the second highest fold change in the pathway "synaptic vesicle" (following the top hit *PARK7*, DJ-1) (Fig. 1C) and the highest fold change in "chemical synaptic transmission" (fig. S4B). The aforementioned AT2A3 displayed the highest fold change among proteins in the pathway "transmembrane transporter binding" (fig. S3B). In addition, numerous other proteins represented in these pathways have crucial roles for the synaptic function and proper vesicle formation. Out of those, examples are SV2B (synaptic versicle glycoprotein 2B) (Fig. 1C and fig. S4B) that is located on synaptic vesicles and involved in neurotransmitter release regulation (*22*) and AT1A1 (alpha-1A subunit of the Na^+/K^+-ATPase) (fig. S3B), an enzyme essential for maintaining the electrochemical gradients across the plasma membrane. Furthermore, SYN1 (synapsin 1) and SYN2 (synapsin 2), primarily involved in the regulation of neurotransmitter release and synaptic vesicle dynamics (*23*, *24*), were found to be less abundant in *DJ-1* KO neurons in our proteomics dataset (Fig. 1C and fig. S4B). Other proteins essential for clathrin-mediated endocytosis, synaptic vesicle recycling, vesicle dynamics, and neurotransmitter release, such as PACN1, RIMB2, RAB3C, or SNP25 (*25*–*27*), were present in low abundance in *DJ-1* KO neurons (Fig. 1C). Beyond alterations in proteins involved in DA uptake, synaptic vesicle dynamics, and neurotransmitter release, *DJ-1* KO neurons also showed impaired calcium handling, including reduced expression of CAC1B [also known as CACNA1B (calcium voltage-gated channel subunit alpha 1B)], which encodes the Cav2.2 subunit of N-type voltage-gated calcium channels (Fig. 1C and figs. S3B and S4B).

Collectively, proteomic profiling of DJ-1–deficient midbrain dopaminergic neurons revealed widespread changes in protein abundance across multiple synapse-associated pathways related to the synaptic vesicle function, neurotransmission, and calcium homeostasis. Among these, the DA vesicle transporter VMAT2 emerged as one of the most strongly down-regulated proteins, suggesting that it may play a central role in the pathogenic cascade associated with midbrain neuron vulnerability.

DJ-1 interacts with vesicular and cytoskeletal components, an association lost in DJ-1–deficient dopaminergic neurons

Given that we found the loss of DJ-1 to interfere with pathways associated with synaptic vesicles, we sought to substantiate this notion with a comparative interactome analysis of DJ-1 via comigration and immunoprecipitation (IP) studies. Therefore, we subjected digitonin-soluble (1%) lysates of *DJ-1* KO and isogenic control neurons to nondenaturing blue-native polyacrylamide gel electrophoresis (BN-PAGE) to visualize and separate multisubunit protein complexes associated with DJ-1 (Fig. 2A). When blotting against DJ-1 after BN-PAGE, we identified a range of native molecular weights with the strongest immunoreactivity in the control neurons physiologically expressing wild-type (WT) DJ-1, and excised four gel blocks (bands A to D) covering this region, which were then processed via in-gel digestion and liquid chromatography–tandem MS (LC-MS/MS) (Fig. 2B and table S2). By comparing the proteomic profiles of control and *DJ-1* KO lysates in each of these bands, we sought to identify potential interactants comigrating with DJ-1 (Fig. 2C and fig. S5A). Through this approach, proteins and protein complexes coincidentally comigrating—but not interacting—with DJ-1 would not be differentially enriched, as we would expect these species to be equally abundant in *DJ-1* KO and control lysates. GO cellular component analysis, using SubcellulaRVis (*28*), of the putative interactants comigrating with DJ-1 unraveled, across all bands, cytoplasmic and nuclear components enriched in control over *DJ-1* KO lysates (Fig. 2D and fig. S5B). In bands “A” and “B,” we also uncovered a substantial number of proteins comigrating with DJ-1 associated with intracellular vesicle compartments (band “A”) and the cytoskeleton (bands “A,” “B,” and “D”) (Fig. 2D and fig. S5B). Peroxisomal proteins were also found to associate with DJ-1 (band “D”; fig. S5B), besides an expected pool of mitochondrial proteins (bands “B” and “C”; Fig. 2D and fig. S5B).

Given that our comigration studies supported the association of DJ-1 with vesicular compartments and vesicle-trafficking machinery, we validated this hypothesis by confirming the physical interaction of DJ-1 with vesicular and endosomal protein components via IP-MS of *DJ-1* KO and isogenic control neuronal lysates using endogenous DJ-1 as our bait (Fig. 2E). On the 221 coimmunoprecipitated proteins (including isoforms not resolved by MS; table S3), we ran a STRING enrichment meta-analysis (*29*), restricting our search to established physical interactions. STRING connected a large number of coimmunoprecipitated proteins to a single network, suggesting that DJ-1 associates with known protein machineries of synaptic and mitochondrial components and highlighting, among these, an enrichment of small Rab guanosine triphosphatases and respiratory chain proteins (Fig. 2F). Notably, cytoplasmic and nuclear components, the top GO hits in our comigration analysis, are much less represented in the co-IPs, where more stringent lysis and wash conditions are applied, suggesting that most of these interactions are very weak and/or spurious. Consistently, subsequent GO cellular component analysis of the coimmunoprecipitated interaction partners of DJ-1 showed the strongest enrichment for proteins associated with intracellular vesicles but also included mitochondria, endosomes, and the cytoskeleton (Fig. 2G). Together, MS analysis after BN-PAGE and co-IP strengthens our whole-cell proteomics results and confirms the association of DJ-1 with vesicular components in midbrain dopaminergic neurons, an association that is lost upon DJ-1 deficiency.

Ultrastructural deficiency of VMAT2 synapses in DJ-1–deficient dopaminergic neurons

While our proteomic analysis uncovered a range of dysregulated proteins and synapse-associated pathways in DJ-1–deficient midbrain dopaminergic neurons, most candidate hits require additional experimental validation. Given that VMAT2 ranked among the top three most down-regulated proteins in our dataset and serves a critical role in midbrain dopaminergic neurons by sequestering DA into synaptic vesicles, thus safeguarding against DA-mediated neurotoxicity, we specifically focused on this transporter in our further analysis. Therefore, as a next step, we aimed to disentangle the consequences of loss of VMAT2 protein in the context of DJ-1 deficiency in dopaminergic neurons on multiple spatial scales using state-of-the-art imaging approaches. First, confocal microscopy analysis revealed a reduced density of VMAT2-positive synapses in *DJ-1* KO neurons compared to the isogenic healthy control neurons (Fig. 3A), while there was no change in the abundance of vesicular GABA (γ-aminobutyric acid) transporter (VGAT)–positive and vesicular glutamate transporter 2 (VGLUT2)–positive synapses (markers of inhibitory GABAergic and excitatory glutamatergic synapses, respectively) that were detected in low amounts in this culture (fig. S6). While the molecular and ultrastructural organization of VGAT- and VGLUT2-positive synapses has been extensively studied, dopaminergic synapses are relatively understudied and the molecular composition and structural signatures are poorly understood.

To obtain a more in-depth analysis of the ultrastructural organization of dopaminergic synapses, we performed recently developed single-molecule localization microscopy (SMLM), three-dimensional (3D) minimal fluorescence photon fluxes (MINFLUX) nanoscopy (*30*, *31*), on identified individual synapses (Fig. 3, B to G). MINFLUX

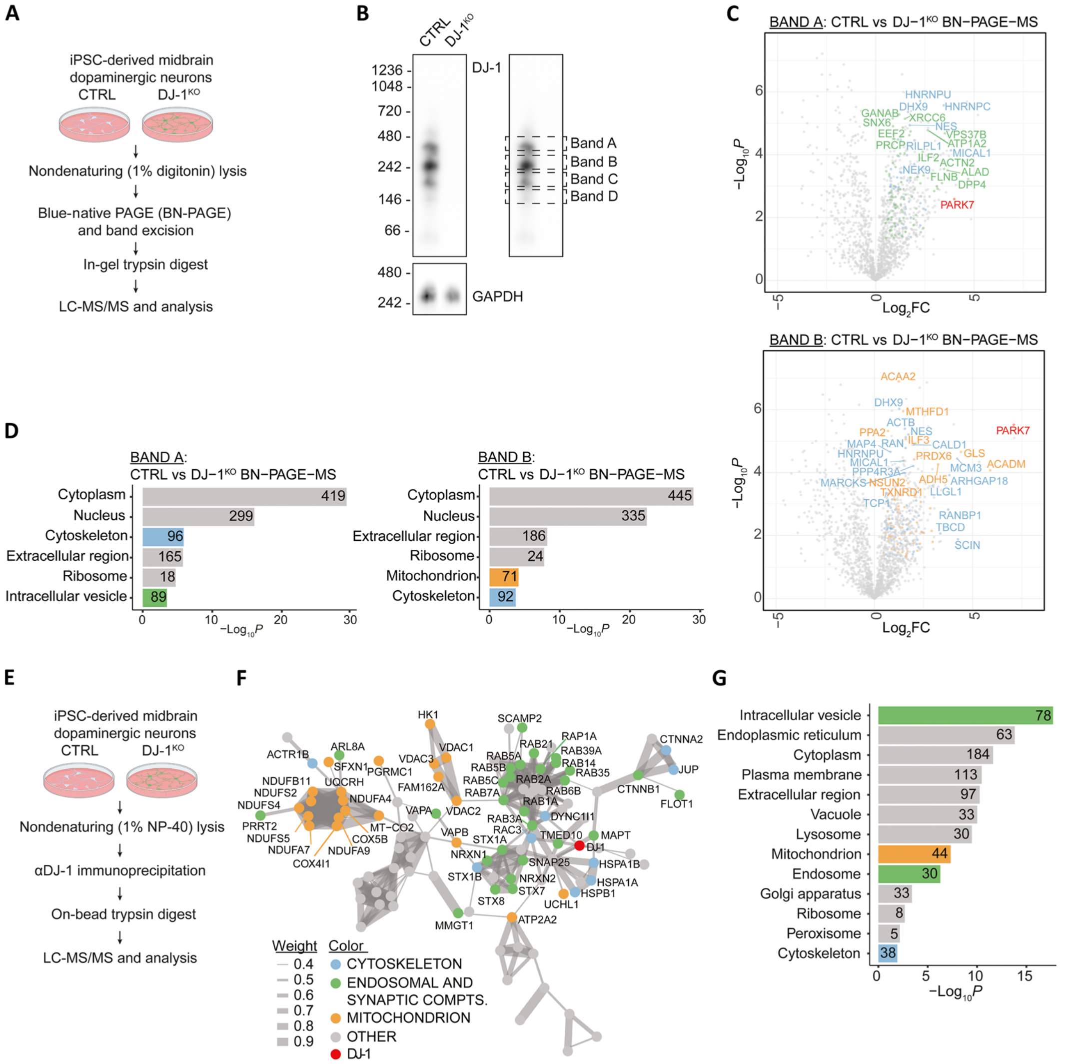

Fig. 2. Vesicular association of DJ-1 as defined by comigration on BN-PAGE and IP-MS. (**A**) Workflow of the comigration experiment (BN-PAGE followed by LC-MS/MS). (**B**) Lysates from control or *DJ-1* KO neurons were separated by BN-PAGE, and four gel bands, covering the region with the strongest DJ-1 immunoreactivity, were excised for LC-MS/MS analysis (bands "A" to "D"). (**C**) Volcano plots of the proteins in bands "A" and "B" comigrating with DJ-1, identified by comparing control to *DJ-1* KO neurons (two-sided t test, $n = 4$ biological replicates). Highlighted are representative DJ-1 comigrants associated with the cytoskeleton (blue), intracellular vesicles (green), and mitochondria (orange). PARK7 (DJ-1) is highlighted in red. (**D**) GO cellular component analysis, using SubcellulaRVis, of DJ-1 comigrants in bands "A" and "B" ($\log_2$FC > 0.5, $P < 0.05$). (**E**) Workflow of the DJ-1 IP-MS experiment. (**F**) STRING enrichment analysis of DJ-1 coimmunoprecipitated ($\log_2$FC > 2 in two of the three biological replicates) proteins. Only experiment- and database-derived physical interactions (confidence ≥0.4) were considered to generate the network, and only the largest connected subnetwork is shown. Color coding as in (C). (**G**) GO cellular component analysis, using SubcellulaRVis, of DJ-1 coimmunoprecipitated proteins ($\log_2$FC > 2 in two of the three biological replicates).

requires minimal photon fluxes from the fluorophores to achieve unprecedented 3D localization precision down to ~1 Å. In this work, we combined MINFLUX with DNA PAINT, another SMLM technique, wherein the transient binding of a dye-labeled imager DNA strand on the target mimics the fluorophore blinking events that are captured in SMLM. Dopaminergic synapses were labeled using a VMAT2 monoclonal primary antibody-secondary nanobody complex carrying a docking strand, while Piccolo, a presynaptic scaffolding protein, was labeled using the conventional primary-secondary antibody complex. Piccolo acted as a marker to identify individual synapses and was imaged in the confocal mode before MINFLUX imaging (Fig. 3E, left). The MINFLUX-DNA PAINT combination markedly reduced the high background signal that is commonly associated in dense structures like synapses and improved the localization precision in both lateral and axial dimensions, leading to a localization precision of individual fluorophores <3 nm in both axial and lateral dimensions (Fig. 3C). Overall, our MINFLUX-DNA PAINT imaging clearly revealed the presynaptic vesicles as clusters of fluorophores organized in 3D within presynaptic boutons (Fig. 3E, right). Such a clear 3D visualization of presynaptic vesicles allowed us to quantify parameters including the total number of VMAT2-positive vesicles per synapse, vesicle diameter, and vesicular density, which are traditionally investigated using transmission electron microscopy (EM). Furthermore, the molecular-level resolution of MINFLUX microscopy enabled the detection of the

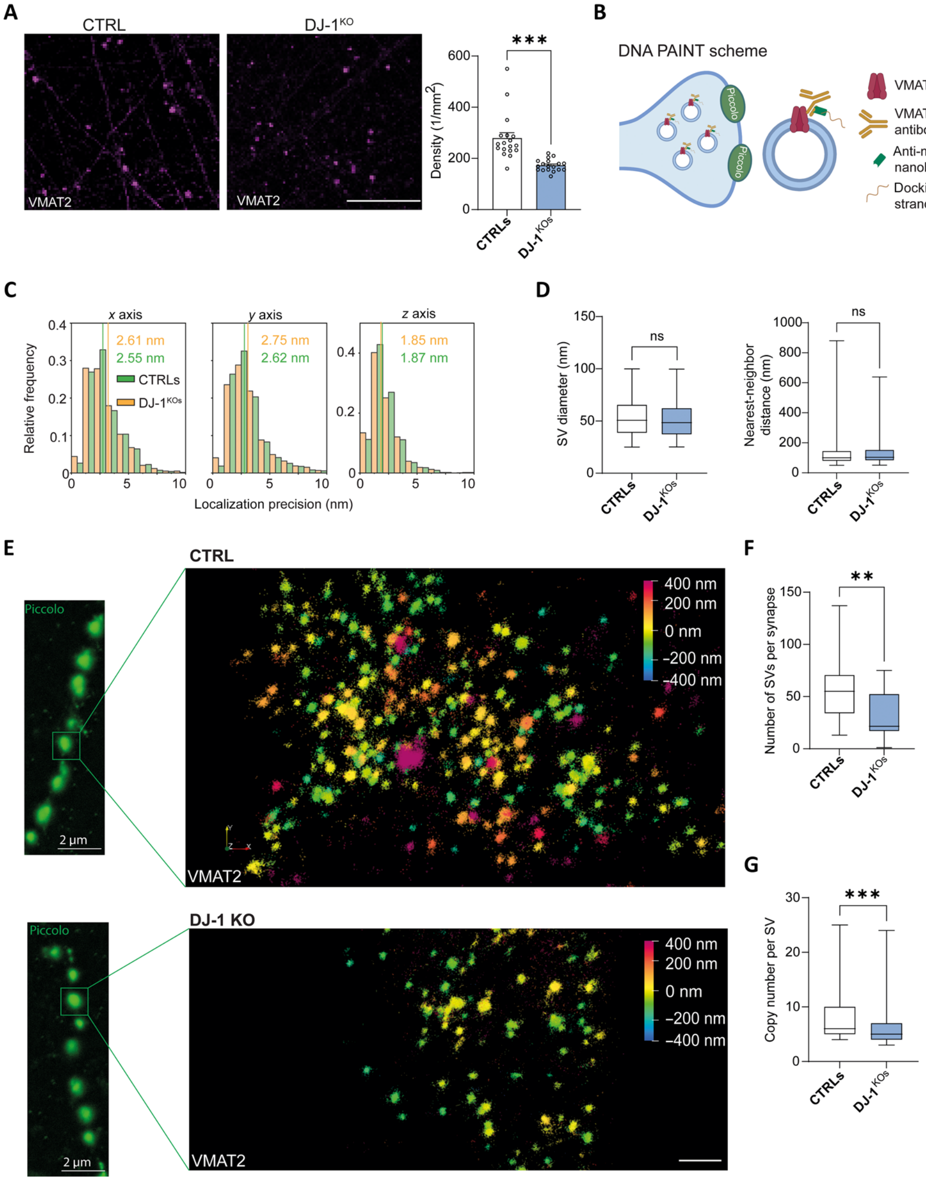

Fig. 3. Ultrastructural deficiency of VMAT2 synapses in DJ-1–deficient dopaminergic neurons. (**A**) Representative confocal images of dopaminergic synapses, visualized by staining VMAT2, in control and *DJ-1* KO neurons. Right, bar graph quantifying the density of synapses per area. Scale bar, 20 μm ($n = 18$). (**B**) Illustration showing MINFLUX-DNA PAINT labeling of VMAT2-positive synapses. Piccolo, the active zone marker, was used to identify synapses before MINFLUX imaging. Created in BioRender. L. F. Burbulla (2026); https://biorender.com/d2ckjpe. (**C**) Histograms showing the distribution of localization precision for VMAT2 MINFLUX imaging in the axial (x and y) and lateral (z) axes. The yellow and green lines indicate the median for control and *DJ-1* KO neurons, respectively. (**D**) Box-whisker plot quantification of the synaptic vesicle (SV) diameter and the nearest-neighbor distance between vesicles in control and *DJ-1* KO neurons ($n = 459$ versus 849 for SV diameter; $n = 594$ versus 1193 for NND). ns, not significant. (**E**) Left, representative confocal image of a dendritic segment showing individual synapses stained by Piccolo. Scale bar, 2 μm. Right, representative MINFLUX raw images of the zoomed-in region from the left panel showing 3D localizations of VMAT2 in a control (top panel) and a *DJ-1* KO neuron (bottom panel). The individual localizations are color coded by their positions in the z-axis. Scale bars, 100 nm (xy) and 800 nm (z). (**F**) Box-whisker plot quantification of the number of synaptic vesicles per synapse in control and *DJ-1* KO neurons ($n = 20$ versus 21). (**G**) Box-whisker plot quantification of the copy number of VMAT2 protein per synaptic vesicle in control and *DJ-1* KO neurons ($n = 558$ versus 1034). $^{**}P < 0.01$; $^{***}P < 0.001$.

copy number of VMAT2 protein per vesicle. Although no difference in the vesicle diameter (Fig. 3D, left) and the distance to the nearest-neighboring synaptic vesicle (Fig. 3D, right) was observed, we found a significant reduction in the total number of VMAT2-positive vesicles per synapse (Fig. 3F) and a reduced VMAT2 protein copy number per vesicle (Fig. 3G) in *DJ-1* KO neurons over controls.

In summary, the insights provided by MINFLUX offer a cutting-edge approach for ultrastructural analysis of neuronal synapses, with the potential to uncover disease-related alterations at the single-molecule level. Thus, MINFLUX imaging revealed that VMAT2 is globally reduced not only at the neuronal level, as shown by whole-cell proteomics, but also at the single synapse and single vesicle levels.

This represents a detrimental disruption of synaptic functionality in DJ-1–deficient neurons.

Reduced sequestration of DA revealed by false neurotransmitter assays and diminished ATP levels in DJ-1–deficient dopaminergic neurons

So far, our results uncovered diminished VMAT2 abundance at molecular, micro-, and nanoscales in *DJ-1* KO neurons when compared to the respective controls. For further experimental analysis, we included another CRISPR-edited cell line and its respective isogenic counterpart by differentiating iPSCs from a patient with PD carrying *PARK7/DJ-1* mutation c.192G>C (DJ-1$^{\text{mut-patient}}$) and its CRISPR-edited control (CTRL$^{\text{mut-edited}}$) (*32*) into midbrain dopaminergic neurons (figs. S1 and S2). Using those three pairs of gene-edited DJ-1–deficient cell lines, we first confirmed the reduced abundance of VMAT2 in *DJ-1* KO neurons (Fig. 4A) as well as in neurons from a patient with DJ-1–linked PD (Fig. 4B) via immunoblotting. While VMAT2 protein levels are an important parameter for neurons that are designed to sequester (and release) the DA neurotransmitter, VMAT2 transport activity is the most predictive determining factor of the efficiency of vesicular DA uptake (*33*, *34*). We therefore assessed VMAT2's activity using a fluorescent false neurotransmitter in fluorometric live-cell assays (*35*–*37*), involving the use of synthetic compounds that mimic the properties of natural neurotransmitters and are therefore valuable tools for studying neurotransmitter dynamics, vesicular release, and synaptic activity in live cells. Using false fluorescent neurotransmitter 206 (FFN206) (*36*), a fluorescent false neurotransmitter probe structurally similar to DA and modified to emit fluorescence when taken up into synaptic vesicles (Fig. 4C), we found the vesicular sequestration capacity of VMAT2 to be diminished in *DJ-1* KO neurons as well as neurons from a patient with DJ-1–linked PD (Fig. 4D), corroborating the impaired VMAT2 expression observed in these neurons. To verify that the transport is mediated through VMAT2 in this experiment, we treated control dopaminergic neurons with the VMAT2 inhibitor tetrabenazine, which, as expected, led to a marked disruption of VMAT2 activity (Fig. 4D).

Diminished VMAT2 activity observed in the fluorometric assay could reflect either the reduced VMAT2 expression levels, an inherent impairment of VMAT2 transport activity, or both. To determine whether VMAT2 activity is, at least in part, involved in this pathology, we assessed whether its transport function is compromised in these neurons. Knowing that proper mitochondrial function and ATP supply are prerequisites for VMAT2 functionality, we first assessed the mitochondrial health using tetramethylrhodamine ethyl ester (TMRE), a mitochondrial membrane potential indicator. Quantification of the percentage of TMRE-labeled mitochondria revealed dysfunctional mitochondria with compromised membrane potential in *DJ-1* KO neurons as well as neurons from a patient with DJ-1–linked PD (Fig. 4E). Next, we examined the levels of ATP using a fluorometric assay and detected reduced ATP in both *DJ-1* KO neurons and neurons derived from a DJ-1–linked PD patient compared to controls, potentially reflecting the result of diminished mitochondrial function (Fig. 4F). Together, our results show that DJ-1–deficient midbrain neurons exhibit both a marked deficiency of VMAT2 protein levels across different scales and severely impaired VMAT2 transport activity, leading to multilevel disturbance to VMAT2-dependent sequestration of DA into synaptic vesicles.

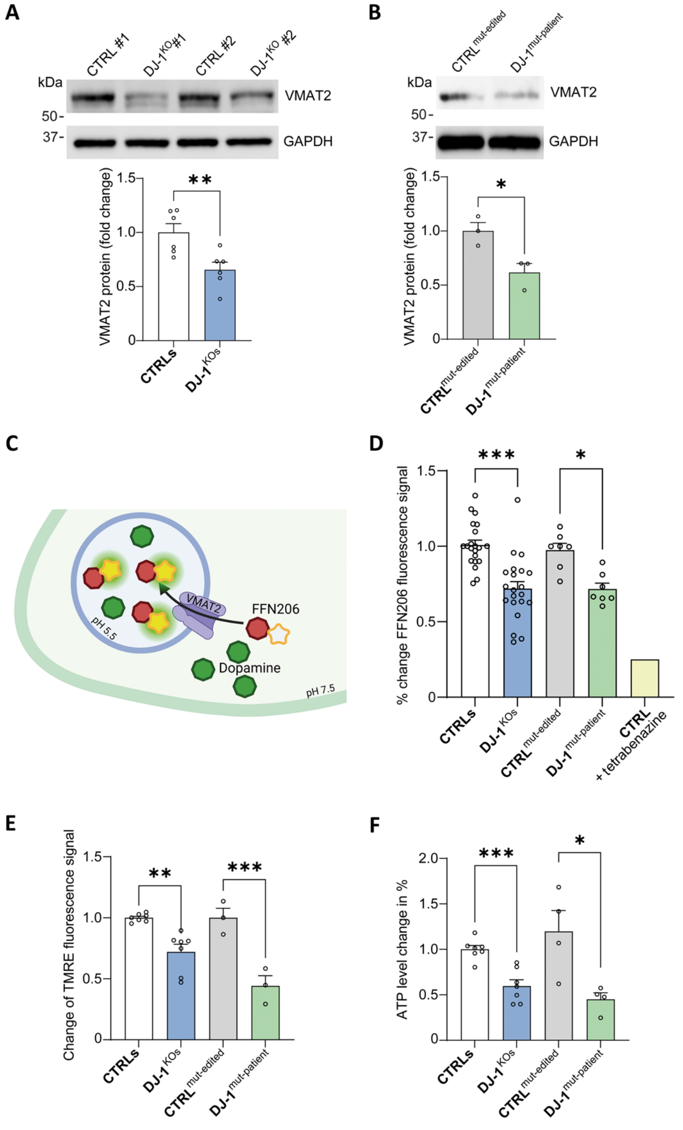

Fig. 4. Reduced sequestration of DA resulting from diminished mitochondrial function and low ATP levels in DJ-1–deficient dopaminergic neurons. (**A** and **B**) Immunoblot analysis of VMAT2 in T-soluble neuronal lysates from (A) *DJ-1* KO and isogenic control neurons ($n = 6$) or (B) neurons from a patient with DJ-1–linked PD and isogenic control neurons ($n = 3$). GAPDH was used as the loading control. (**C**) Schematic diagram of the false neurotransmitter illustrating the presynaptic neuron with the synaptic vesicle represented in blue, DA as green circles, and the false neurotransmitter as red circles. Following vesicular sequestration of the false neurotransmitter through VMAT2, fluorescence is initiated (yellow glow attached to the false neurotransmitter as a red circle) through a drop in pH and can be quantified using a microplate reader. Created in BioRender. L. F. Burbulla (2026); https://biorender.com/jyr70mp. (**D**) Quantification of the dynamics of intraluminal DA loading by the false neurotransmitter assay of *DJ-1* KO and isogenic control neurons or neurons from a patient with DJ-1–linked PD and isogenic control neurons. Tetrabenazine was used to inhibit VMAT2 activity as control experiment ($n = 7$ to 21). (**E**) Measurement of the TMRE fluorescence signal of *DJ-1* KO and isogenic control neurons or neurons from a patient with DJ-1–linked PD and isogenic control neurons. TMRE fluorescence correlates with mitochondrial membrane potential. The results were normalized to the MitoTracker signal ($n = 3$ to 7). (**F**) Measurement of ATP levels in *DJ-1* KO and isogenic control neurons or neurons from a patient with DJ-1–linked PD and isogenic control neurons ($n = 4$ to 7). $^{*}P < 0.05$; $^{**}P < 0.01$; $^{***}P < 0.001$.

Analysis of the synaptic vesicle ultrastructure uncovers morphological abnormalities in DJ-1–deficient dopaminergic neurons

The identified numerical differences of VMAT2-positive synapses and single vesicles led us to investigate synaptic terminals at a higher resolution to ultrastructurally analyze the morphology of synaptic vesicles using transmission EM. While control neuron terminals contained similarly sized and uniform synaptic vesicles (Fig. 5A), *DJ-1* KO neuron terminals exhibited a variety of abnormally large-sized synaptic vesicles (Fig. 5B). This observation is further supported by the MINFLUX data, which detected nearly twice as many abnormally sized vesicles (>100 nm in diameter) in *DJ-1* KO neurons when compared to isogenic control neurons (Fig. 5C). Notably, in the EM images of *DJ-1* KO neurons, we also observed the presence of intriguing tubular structures within synaptic terminals (Fig. 5B), which were absent in the control neurons.

Our results derived from EM and MINFLUX imaging analysis uncovered an abnormal vesicle morphology in *DJ-1* KO neuron synapses. We hypothesized that these defects originate from potential aberrant regulation in synaptic vesicle endocytosis and recycling, the pivotal local phenomenon that underlies the formation of new synaptic vesicles. In particular, the uncoating process of a newly endocytosed vesicle requires ATP-derived energy to dissociate the clathrin coat, a key protein involved in vesicle endocytosis, by retrieving vesicle components from the plasma membrane through the assembly of clathrin-coated pits (*38*) from the vesicle. Defective clathrin function can result in vesicles with abnormal shapes or sizes, disrupting their ability to efficiently store and release neurotransmitters (*39*). We assessed clathrin levels by immunoblotting and found that the abundance of clathrin was approximately doubled in *DJ-1* KO neurons and neurons from a patient with DJ-1–linked PD compared to their respective controls (Fig. 5D). Overall, the above results suggest that, besides the deficits in VMAT2 abundance and functionality, various morphological abnormalities of synaptic vesicles were also present in DJ-1–deficient neuron synapses, possibly due to a disruption in the vesicle recycling pathways.

Oxidized DA and α-synuclein pathology in DJ-1–deficient dopaminergic neurons

As a next step, we aimed at disentangling pathological consequences of loss of DJ-1 that may be related to the decreased abundance of VMAT2-positive vesicles and synapses, its diminished function, and

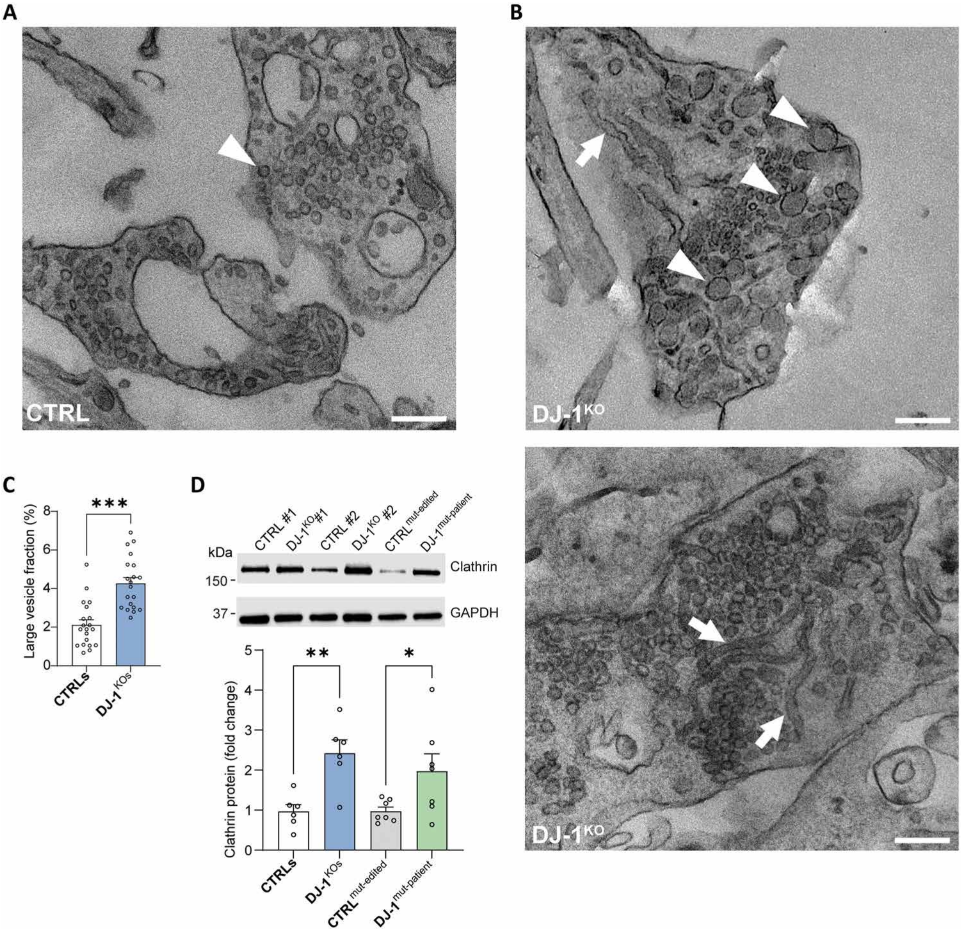

Fig. 5. Morphological abnormalities of synaptic vesicles and excess clathrin in DJ-1–deficient dopaminergic neurons. (**A** and **B**) Representative transmission EM image depicting (A) regular-sized synaptic vesicles (arrowhead) in control neurons and (B) enlarged (arrowheads) or tubular (arrows) synaptic vesicles in *DJ-1* KO neurons. Scale bars, 200 nm. (**C**) Quantification of the large vesicle fraction (i.e., structures with a diameter of >100 nm) in dopaminergic synapses of control and *DJ-1* KO neurons ($n = 20$). (**D**) Immunoblot analysis of clathrin in T-soluble neuronal lysates from *DJ-1* KO and isogenic control neurons or neurons from a patient with DJ-1–linked PD and isogenic control neurons ($n = 6$ or 7). GAPDH was used as the loading control. *$P < 0.05$; **$P < 0.01$; ***$P < 0.001$.

the observed structural vesicular abnormalities. A direct consequence of those outlined vesicular deficits is the partial loss of the capacity to sequester DA, which would in turn remain cytosolic and oxidize over time. Using a near-infrared fluorescence (nIRF) assay to visualize oxidized DA (*40*), we found elevated levels of DA oxidation in both *DJ-1* KO neurons and neurons derived from a patient with DJ-1–linked PD (Fig. 6A).

While the loss of DJ-1 led to a reduction of VMAT2 protein levels and DA oxidation in human neurons, the lack of DJ-1 in analogous iPSC-derived mouse dopaminergic neurons generated from *DJ-1* KO mouse embryonic fibroblasts (MEFs) (fig. S7, A to D) resulted in a similar reduction of VMAT2 protein in immunoblotting (fig. S7E) but no DA oxidation using nIRF assay (fig. S7F) compared to WT mouse iPSC-derived dopaminergic neurons. The latter result is in accordance with our previously published work (*3*).

Increased levels of cytosolic DA, oxidized DA accumulation, and DA-protein adduct formation are implicated in the covalent modification and aggregation of α-synuclein, the primary structural component of Lewy bodies and a key pathological feature of PD (*41*–*43*). Recent studies have linked the loss of DJ-1 function to the accumulation of various forms of α-synuclein including oxidized α-synuclein (*3*) and the formation of Lewy bodies (*44*, *45*). By using antibodies against all forms of α-synuclein (C20 antibody) or specific to pathogenically oxidized/nitrated (syn303 antibody) α-synuclein, we found α-synuclein to be elevated in *DJ-1* KO neurons and neurons from a patient with DJ-1–linked PD compared to their respective isogenic controls (Fig. 6B).

In summary, DA oxidation and α-synuclein pathology were found in DJ-1–deficient neurons—both phenotypes that could potentially arise from a shortage of VMAT2-positive vesicles, deficits in the functionality of VMAT2, or altered vesicle recycling. These scenarios are known to affect the proper vesicular uptake of DA from the cytosol, making it prone to oxidation and potentially interfering with α-synuclein.

ATP treatment alleviates pathologies in DJ-1–deficient dopaminergic neurons

It has been shown in various cell and animal models that the loss of DJ-1 results in mitochondrial defects and that those deficits can potentially result in a decrease in ATP (*46*–*49*). Our study confirmed these discrepancies in mitochondrial function and ATP levels upon the loss of DJ-1 and further highlighted downstream consequences including α-synuclein pathology and DA oxidation.

Next, as a rescue strategy, we supplemented *DJ-1* KO neurons and neurons from a patient who has DJ-1–linked PD with ATP, directly transferred from the extracellular space into the cell by nucleoside transporters, by nucleotide channels, or through micropinocytosis (*50*–*52*). Treatment of *DJ-1* KO neurons and neurons from a DJ-1–linked PD patient with ATP led to an increase in fluorescent false neurotransmitter signal in fluorometric live-cell assays, indicating increased VMAT2 transporter activity (Fig. 7A). As a proof of concept that the observed effects on replenished VMAT2 functioning were directly linked to supplemented ATP, we treated DJ-1–deficient neurons with adenosine 5′-(γ-thio)-triphosphate (ATP-γ-S), a nonhydrolyzable analog of ATP, thought to fail to deliver the required energy for vesicular sequestration of DA. DJ-1–deficient neurons supplemented with ATP-γ-S showed no change in fluorescent false neurotransmitter signal compared to carrier-treated counterparts (Fig. 7B). We wondered whether the observed elevated levels of clathrin in DJ-1–deficient neurons would also be alleviated upon ATP supplementation. Addition of ATP lowered

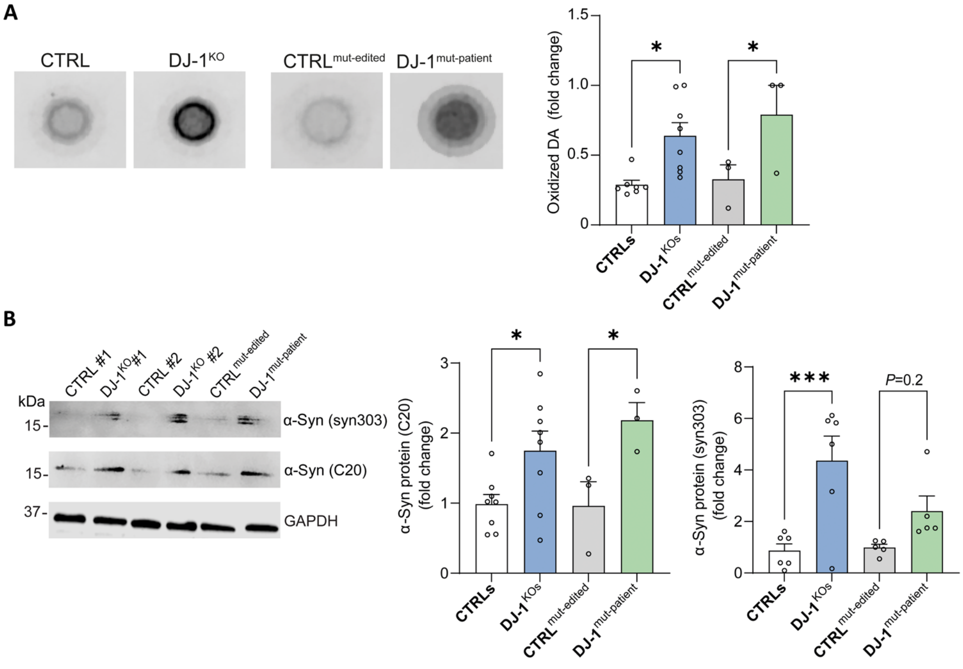

Fig. 6. Oxidized DA and α-synuclein pathology in DJ-1–deficient dopaminergic neurons. (**A**) Representative images of oxidized DA by nIRF in *DJ-1* KO and isogenic human control neurons (left pair) or neurons from a patient with DJ-1–linked PD and isogenic control neurons (right pair) and quantification ($n = 3$ to 8). (**B**) Immunoblot analysis of all forms of α-synuclein (C20 antibody) or oxidized/nitrated forms of α-synuclein (syn303 antibody) in T-soluble neuronal lysates from *DJ-1* KO and isogenic control neurons or neurons from a patient with DJ-1–linked PD and isogenic control neurons and quantification ($n = 3$ to 8). GAPDH was used as the loading control. $^*P < 0.05$; $^{***}P < 0.001$.

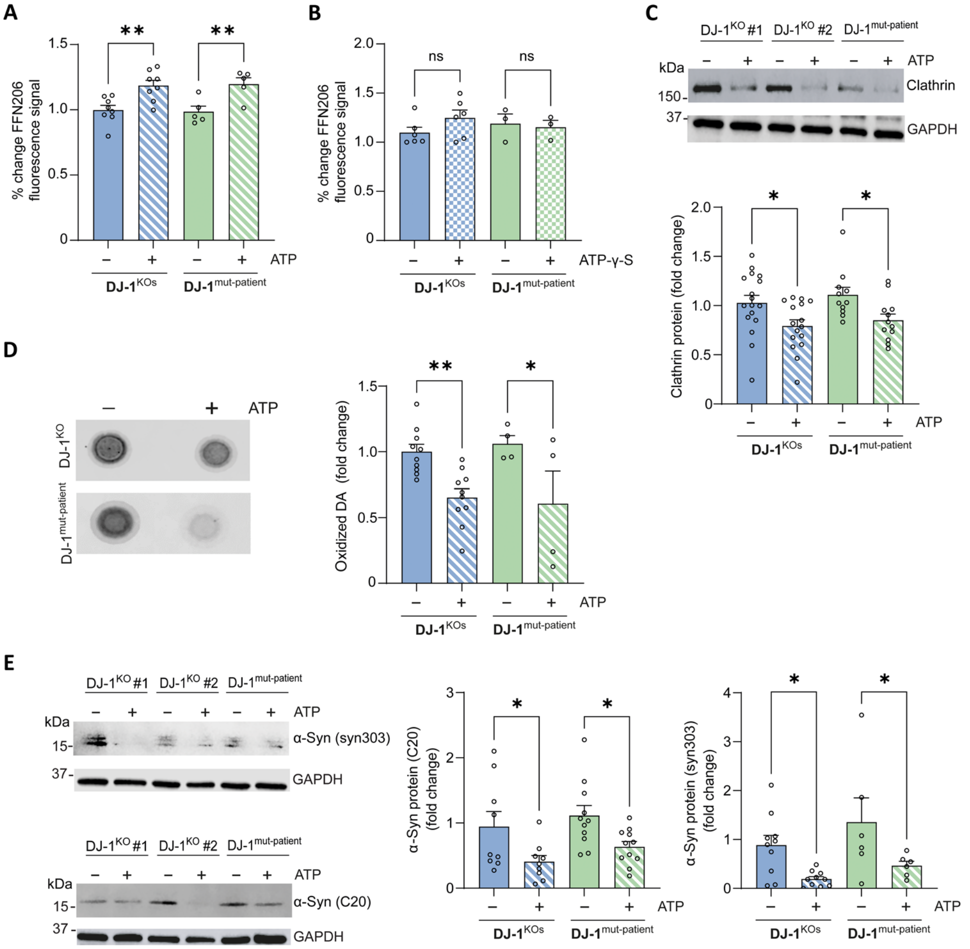

Fig. 7. ATP supplementation lowers clathrin levels, oxidized DA, and α-synuclein pathology by increasing vesicular DA sequestration in DJ-1–deficient dopaminergic neurons. (**A** and **B**) Quantification of the dynamics of intraluminal DA loading by the false neurotransmitter assay of *DJ-1* KO neurons and neurons from a patient with DJ-1–linked PD treated with (A) ATP or carrier H_2O ($n = 5$ to 8) or (B) ATP-γ-S, a nonhydrolyzable analog of ATP, or carrier H_2O ($n = 3$ to 6). (**C**) Immunoblot analysis of clathrin in T-soluble neuronal lysates from *DJ-1* KO neurons and neurons from a patient with DJ-1–linked PD treated with ATP or carrier H_2O and quantification ($n = 12$ to 17). GAPDH was used as the loading control. (**D**) Representative images of oxidized DA by nIRF in *DJ-1* KO neurons (top row) and neurons from a patient with DJ-1–linked PD (bottom row) treated with ATP or carrier H_2O and quantification ($n = 4$ to 10). (**E**) Immunoblot analysis of all forms of α-synuclein (C20 antibody) or oxidized/nitrated forms of α-synuclein (syn303 antibody) in T-soluble neuronal lysates from *DJ-1* KO neurons or neurons from a patient with DJ-1–linked PD treated with ATP or carrier H_2O and quantification ($n = 6$ to 11). GAPDH was used as the loading control. $^*P < 0.05$; $^{**}P < 0.01$.

clathrin protein levels in all DJ-1–deficient lines (Fig. 7C). Knowing that VMAT2 activity and vesicle uncoating of clathrin—both processes that are ATP-dependent and interrupted in DJ-1–deficient neurons—may be potential causes for the observed DA oxidation, we treated *DJ-1* KO neurons and neurons from a patient who has DJ-1–linked PD with ATP and measured oxidized DA by nIRF. We found that DA oxidation was successfully reduced after ATP treatment in all DJ-1–deficient lines (Fig. 7D). ATP treatment also reduced the pathologically elevated levels of α-synuclein in all DJ-1–deficient neuronal lines (Fig. 7E).

In summary, supplementation of ATP reduces downstream pathologies of diminished VMAT2 function, elevated clathrin and α-synuclein, and DA oxidation in DJ-1–deficient neurons. Overall, our results reveal that the loss of DJ-1 leads to DA oxidation and α-synuclein elevation as downstream pathologies of the deficient vesicular uptake of DA, resulting from multiple deficits in the structure and function of VMAT2-positive synapses and vesicles and possibly inefficient uncoating of clathrin-coated vesicles in midbrain neurons (Fig. 8).

DISCUSSION

In this study, we demonstrate that disrupted vesicular sequestration of DA in DJ-1–deficient midbrain dopaminergic neurons contributes to the accumulation of oxidized DA and α-synuclein pathology, key drivers of PD pathogenesis. A large body of evidence links mitochondrial dysfunction to pathology (*53*), yet the precise link to DA oxidation remained unclear. Our work provides a mechanistic explanation by linking the loss of ATP and vesicular dysfunction to this pathogenic process. These findings have substantial implications for future therapeutic strategies targeting DA oxidation and synaptic vesicle integrity in PD.

We applied state-of-the-art imaging approaches including MINFLUX nanoscopy, EM, ultrasensitive DA-specific fluorescent probes, and unbiased as well as targeted proteomic analyses to quantify disturbances of synaptic vesicle function upon loss of the PD-associated protein DJ-1 in three pairs of CRISPR-edited cell lines with their respective isogenic counterparts. Whole-cell proteomics and MS following

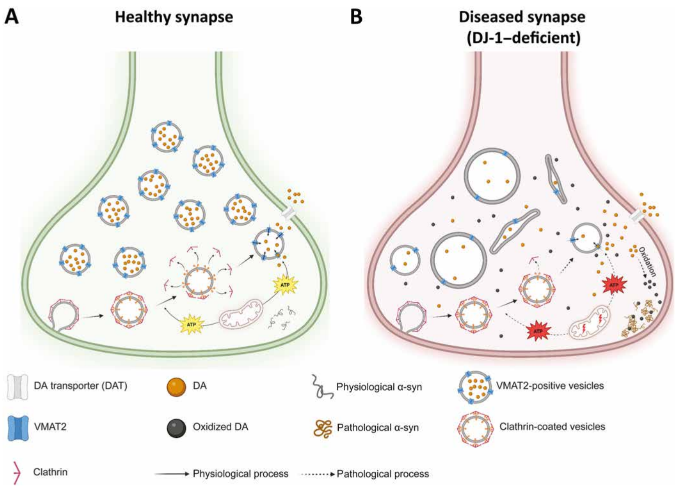

Fig. 8. Deficient uptake of DA into synaptic vesicles of human midbrain neurons results in DA oxidation and α-synuclein pathology. (**A**) In a healthy synapse, clathrin-coated vesicles are being endocytosed, the clathrin coat is being released, and cytosolic DA is being packaged into synaptic vesicles via transport through VMAT2. Both processes, VMAT2-dependent vesicular sequestration of DA and uncoating of clathrin-coated vesicles, rely on the delivery of energy through sufficient ATP supply from mitochondrial sources. In this physiological situation, α-synuclein protein is present in its soluble monomeric form. Created in BioRender. L. F. Burbulla (2026); https://biorender.com/3cqppxt. (**B**) In a diseased synapse, under the pathological condition of DJ-1 deficiency, VMAT2-dependent vesicular sequestration of DA is interrupted by several synaptic pathologies. First, the VMAT2 molecule number on each synaptic vesicle is diminished, and the VMAT2-positive vesicle number is lowered. Second, the mitochondrial function is disrupted, leading to insufficient supply of ATP for processes that require energy to function. One consequence of ATP depletion is the inadequate removal of clathrin from clathrin-coated vesicles, triggering abnormally formed (enlarged and tubular) vesicle structures. The other detrimental result of lowered ATP is a functional disruption of VMTA2 activity that is incapable of transporting cytosolic DA into the vesicle lumen for sequestration. These pathologies together lead to an increase in cytosolic DA that is rapidly converted into oxidized forms of DA, further causing neural toxicity and synaptic dysfunction, as also shown by elevated levels of pathological α-synuclein species. Conclusively, the loss of DJ-1 is linked to DA oxidation and α-synuclein pathology in midbrain neurons and connects these downstream pathologies to synaptic disturbances, in particular deficits in the vesicular uptake of DA and vesicle structure. Created in BioRender. L. F. Burbulla (2026); https://biorender.com/nnfiz0i.

BN-PAGE and IP all indicated synaptic vesicle integrity to be affected in neurons lacking DJ-1, with VMAT2 being a key protein found to be substantially reduced.

The role of VMAT2 in DA regulation and neuroprotection remains a topic of active investigation and debate (*54*, *55*). Notably, VMAT2 has been shown to be markedly reduced in the brain of a patient with idiopathic PD, correlating with disease severity (*56*), and synaptic vesicles isolated from human brain tissue demonstrate a reduced DA uptake capability that correlated with impaired VMAT2 activity (*17*). Regions more resilient to degeneration in PD such as the neighboring ventral tegmental area tend to exhibit higher VMAT2 expression levels, suggesting a neuroprotective role (*57*). This study also emphasizes an inverse correlation between the accumulation of the characteristic pigment NM—which forms when excess cytosolic DA is present (*10*)—and VMAT2 levels, suggesting that human nigral neurons accumulate the most NM pigment, in part, because they have the least VMAT2 protein. In line with this, a specific VMAT2 gain-of-function haplotype has been associated with a reduced risk for the development of PD (*58*). Notably, beyond DA oxidation alone, reduced VMAT2 activity increases cytosolic DA metabolism by monoamine oxidase, generating toxic aldehydes like 3,4-dihydroxyphenylacetaldehyde (DOPAL). DOPAL is highly reactive, forms adducts with proteins, promotes α-synuclein aggregation, and enhances mitochondrial dysfunction, thereby representing a critical additional mediator of dopaminergic neuron toxicity (*17*, *59*).

In addition to this, numerous in vivo studies demonstrate the critical role of VMAT2 deficiency in DA regulation. While heterozygous VMAT2 KO mice do not show locomotor deficits or neuron degeneration at the baseline, they exhibit increased striatal contents of DA and, upon treatment with dopaminergic toxins, signs of Parkinson-like neurodegeneration (*60*). Conditional KO models with VMAT2 deletion specific to the nigrostriatal pathway show striatal DA depletion, motor deficits, weight loss, and accelerated death but, again, no degeneration of nigrostriatal neurons (*61*). Viral-mediated interference of VMAT2 expression in transduced dopaminergic cell bodies in the SN of adult rats recapitulates key pathological features such as dysregulated cytosolic DA indicated by a reduction of striatal DA, with a corresponding increase in DA turnover as well as elevated levels of protein cysteinyl-DA adducts, and degeneration of nigrostriatal dopaminergic neurons (*54*). Elevated cysteinyl-catechols were also observed in mice with a residual 5% expression of VMAT2 and a reduction of TH-positive fiber density in aged mice (*62*).

Together, these human and rodent studies support our hypothesis that reduced VMAT2 levels or functionality impairs DA sequestration and homeostasis. However, the loss of VMAT2 in mice does not necessarily lead to nigrostriatal degeneration. While some of the mentioned studies show nigrostriatal neurodegeneration upon the loss of VMAT2, others report no evidence for the loss of SN neurons with the deficiency of VMAT2, highlighting the variability and heterogeneity between animal models. Underlying species-specific differences of DA regulation in the nigrostriatal system may account for this difference, which requires further mechanistic investigations.

It has been shown that small interfering RNA–mediated reduction of DJ-1 levels resulted in reduced VMAT2 levels, although these results were solely collected under knockdown conditions in a human neuroblastoma cell line under naïve, undifferentiated conditions (*18*, *63*). Nevertheless, these results suggest that, at least in neuroblastoma cells, DJ-1 positively regulates VMAT2 expression and suggests a more general role of DJ-1 in regulating VMAT2 levels. This rather universal association between DJ-1 and VMAT2 may also explain our results on comparable VMAT2 reduction in human and mouse iPSC-derived *DJ-1* KO neurons. However, while reduction of VMAT2 protein was similar between the species, only the loss of DJ-1 in human, but not mouse, dopaminergic neurons resulted in an accumulation of oxidized DA. This is in line with the fact that rodents do not form NM in SN under physiological conditions (*64*, *65*) and in line with our previous study showing that oxidized DA does not accumulate in mouse SN brain tissue or iPSC-derived mouse dopaminergic neurons (*3*) and underscores the notion that also major PD pathologies, such as substantial neuron loss, are absent in *DJ-1* KO mouse models (*66*–*68*). While the underlying species-specific differences that lead to the lack of this human-specific pathology are still unclear, one potential reason for DA oxidation reflecting a species-specific difference may be the ability of the murine system to compensate for a reduction in VMAT2 through other, yet unknown, mechanisms. While more research needs to be done to understand the association between DJ-1 and VMAT2 in disease-relevant model systems, our own findings strengthen the link between DJ-1 deficiency, diminished VMAT2-dependent vesicular sequestration, and toxic DA oxidation in synapses of vulnerable human midbrain neurons.

Besides the observed VMAT2 transporter (activity) disturbances, another intriguing phenotype of synaptic integrity was the disrupted vesicle morphology. The underlying reasons for the observed irregular vesicle formations are unclear and need more investigation. However, the overabundance of clathrin in DJ-1–deficient neurons suggests that clathrin removal from clathrin-coated vesicles is impaired. This inadequate removal might trigger the formation of abnormally shaped (enlarged and tubular) vesicle structures that may represent morphologically altered synaptic vesicles or tubulovesicular membranes resembling endosomes (*69*). Clearly, both pathologies—VMAT2 deficiency and irregular vesicle morphology—impair the uptake of DA into vesicles of DJ-1–deficient midbrain synapses, leading to the buildup of unsequestered DA in the cytosol, which is susceptible to oxidation (Fig. 8).

Oxidized DA is a highly neurotoxic compound and has been shown to be able to modify proteins, including α-synuclein (*41*, *42*). In our study, we also found forms of α-synuclein, including the oxidatively modified forms, to be increased in DJ-1–deficient neurons. α-Synuclein, a natively unfolded protein predominantly localized to the presynaptic terminal, has been extensively studied in PD (*70*). Under pathological conditions, α-synuclein is often found abnormally phosphorylated, ubiquitinated, oxidized, and nitrated (*71*), and these toxic α-synuclein species impair the cellular function and survival (*72*). There is evidence for a role of DJ-1 in inhibiting the initial aggregation of α-synuclein monomers through its molecular chaperone-like activity (*73*, *74*). Furthermore, research has shown that the loss of DJ-1 leads to an increase in aggregated α-synuclein levels in both cell and animal models of PD (*75*). In this regard, the presence of pathologic α-synuclein oligomers has been shown to initiate down-regulation of synapsins, i.e., SYN1 and SYN2, primarily involved in the regulation of neurotransmitter release and synaptic vesicle dynamics (*76*). Our proteomic whole-cell analysis revealed both SYN1 and SYN2 to be less abundant in DJ-1–deficient neurons. This highlights the possibility of a toxic feedforward loop of deficient vesicular sequestration, leading to DA oxidation and α-synuclein accumulation, that in turn may affect the vesicular uptake of DA by affecting synapsin levels and, over time, enhance the level of neuron vulnerability. In addition, proteomics revealed reduced calcium ion binding in *DJ-1* KO neurons, suggesting a previously underappreciated role for DJ-1 in presynaptic calcium regulation. This aligns with the findings of Guzman *et al.* (*13*), who demonstrated that DJ-1 attenuates oxidant stress generated by calcium-dependent pacemaking activity in dopaminergic neurons. Our data may indicate that the loss of DJ-1 compromises calcium buffering or signaling, possibly making neurons more vulnerable to oxidative stress.

Although mutations in *DJ-1* are a rare cause of familial PD, accumulating evidence supports a broader relevance of DJ-1 to idiopathic forms of PD. Oxidized DJ-1 protein has been detected in postmortem brain tissues of patients with sporadic PD (*77*), suggesting that DJ-1 undergoes pathological modifications that may impair its function. This loss or reduction of DJ-1 functionality resulting from oxidative damage could contribute to neuronal vulnerability beyond genetically defined cases, positioning DJ-1 as a potential common mediator of PD pathogenesis.

Moreover, DJ-1 plays a critical role in mitochondrial quality control and cellular antioxidant responses (*48*, *49*, *78*). Mitochondrial dysfunction and consequent ATP deficiency are established hallmarks of both familial PD and sporadic PD, contributing to synaptic dysfunction, increased oxidative stress, and dopaminergic neurodegeneration (*79*–*81*). By modeling DJ-1 deficiency, we recapitulate these key features of impaired mitochondrial bioenergetics and oxidative stress, establishing a framework applicable to a wider spectrum of PD cases. Thus, DJ-1–deficient iPSC-derived dopaminergic neurons serve as a valuable model to investigate convergent pathological mechanisms centered around mitochondrial dysfunction and DA oxidation that are shared by diverse PD etiologies.

Compounds, such as 1-methyl-4-phenyl-1,2,3,6-tetrahydropyridine (MPTP), rotenone, and paraquat, that are known to interfere with the mitochondrial function and induce PD-like symptoms have been used to generate neurotoxic models of PD since decades (*53*). Notably, energy defects and diminished ATP production have been observed in patients with PD and linked to α-synuclein aggregation (*82*, *83*). Mitochondrial dysfunction has been detected even before α-synuclein aggregation or neurodegeneration, suggesting it being a potential causal trigger or even an initiator of the disease pathology (*84*) and of the toxic cascade described in our study (Fig. 8).

The question of how such a neurotoxic feedforward loop was initiated in DJ-1–deficient neurons remains. Broad evidence from diverse experimental models supports mitochondrial dysfunction concomitant with reduced ATP levels upon the loss of DJ-1 (*13*, *46*–*49*). This loss of ATP is particularly problematic in dopaminergic neurons, which rely on this source of energy for critical processes, including VMAT2 activity and uncoating of clathrin-coated vesicles. All DJ-1–deficient lines in our study exhibited reduced mitochondrial membrane potential and ATP levels. Therefore, as a proof-of-concept experimental model, we aimed at interrupting the initiation of this toxic cycle and supplemented DJ-1–deficient neurons with ATP. This strategy uses the residual, well-functioning VMAT2 molecules to package cytosolic DA into synaptic vesicles, thereby mitigating the risk of oxidation. ATP treatment successfully rescued the observed pathologies, including diminished VMAT2 transporter activity, DA oxidation, and elevated α-synuclein levels. The ATP-mediated restoration of VMAT2 function implies suboptimal transporter activity, potentially reflecting proton gradient dissipation or partial uncoupling between vacuolar ATPase and VMAT2. This interpretation aligns with the essential role of the proton electrochemical gradient for proper VMAT2-mediated vesicular uptake, which may be compromised in DJ-1 deficiency. However, direct assessment of proton gradient dynamics within synaptic vesicles remains technically challenging. While genetically encoded pHluorins have provided valuable insights into synaptic vesicle pH regulation (*85*), limitations in spatial resolution resulting from imaging techniques and potential variability in specificity persist. Moreover, the use of pH-sensitive fluorescent false neurotransmitter probes offers an alternative approach but is complicated by interpretational ambiguities, as probe uptake depends on VMAT2 activity, which is diminished in this context. Our ATP supplementation strategy thus represents a useful mechanistic tool revealing VMAT2 dysfunction possibly linked to proton gradient uncoupling, but further studies using refined imaging techniques and more sensitive probes will be essential to resolve these mechanistic details.

While our study reveals important insights into VMAT2 deficiency and synaptic vesicle dysfunction in DJ-1–deficient dopaminergic neurons, several limitations should be acknowledged. First, our analyses were conducted using iPSC-derived dopaminergic neurons from only a limited number of *DJ-1* KO and patient lines. Future studies including a larger group of patient samples with diverse genetic backgrounds will be important to better reflect patient variability and to confirm the consistency of these findings across diverse PD etiologies. Second, supplementation of ATP has been used in our study as an experimental model, and although effective as a proof of principle, this approach represents an artificial strategy of bioenergetic support. While improving the mitochondrial function remains a key therapeutic target in PD, most clinical trials targeting brain energetics have not met key clinical endpoints (*53*). Still, much of the research is in early stages, and further studies are needed to fully understand how mitochondrial modulators can be effectively applied in clinical settings. Last, the use of 2D cultured human midbrain dopaminergic neurons primarily addresses cell-autonomous dysfunction, lacking the physiological complexity of neuronal circuits and diverse brain cell types that likely contribute to PD pathogenesis in vivo. Additional validation in humanized or patient-derived models incorporating these complexities (e.g., brain organoids) will be critical to fully elucidate these pathways and advance therapeutic development. In summary, our study marks a substantial step in unraveling the complexities of DA metabolism in human midbrain neurons and opens previously unknown avenues for the development of interventions tailored to dysfunctional pathways of vesicular DA sequestration.

MATERIALS AND METHODS

Culture and characterization of human iPSCs and differentiation into midbrain dopaminergic neurons

We used iPSC lines that were already generated from fibroblasts from one patient with DJ-1–linked familial PD (DJ-1$^{\text{mut-patient}}$) carrying the homozygous c.192G>C mutation in *PARK7* (DJ-1) that was clinically characterized previously (*32*) and its isogenic CRISPR-edited control (CTRL$^{\text{mut-edited}}$) and from two separate healthy control individuals (CTRLs) (*3*, *86*–*88*) and their isogenic PARK7/DJ-1 KO counterparts (*DJ-1* KOs) (*3*). CRISPR-Cas9 gene editing strategies were described previously (*3*, *32*). The study was approved by the Ethics Committee of the Medical Faculty of LMU Munich, Germany (approval number 25-0153). All patients and controls gave written and informed consent.

iPSC cultures were kept on plates coated with Cultrex (R&D Systems, no. 3434-005-02), and the antibiotic-free mTESR Plus medium (Stemcell Technologies, no. 100-0276) was replenished every 2 days. Cells were passaged manually every 5 to 7 days. Each line was assessed for the expression of pluripotency markers by immunocytochemical analysis [Oct4 (Abcam, no. ab19857, 1:200), SOX2 (Abcam, no. ab79351, 1:200), Nanog (Abcam, no. ab80892, 1:200), and SSEA-4 (Millipore, no. MAB4304 at 1:200)], as well as for in vitro differentiation via embryoid body (EB) formation (see below). In addition, all lines were regularly screened for mycoplasma contamination.

The terminal differentiation of human iPSCs into midbrain dopaminergic neurons was conducted according to previously established protocols (*3*, *89*). In summary, once the cells achieved more than 95% confluence (day 0), a differentiation medium comprising Knockout Dulbecco's modified Eagle's medium (DMEM) (Thermo Fisher Scientific, no. 10829-018), KnockOut Serum Replacement (Thermo Fisher Scientific, no. 10828-028), 1% L-glutamine, 1% penicillin-streptomycin (PenStrep), 1% MEM Non-Essential Amino Acids (Thermo Fisher Scientific, no. 11140-050), and 1 mM β-mercaptoethanol (KSR media) was introduced. From days 5 to 10, the cells were transitioned to Neurobasal media (Thermo Fisher Scientific, no. 21103049) enriched with Neurocult SM1 (Stemcell Technologies, no. 5711), 1× PenStrep, and 1× L-glutamine (NbSm1 media). During days 11 to 14, the cells were passaged en bloc in 1- to 2-mm pieces and transferred onto 10-cm dishes coated with poly-D-lysine (PDL)/laminin, continuing to be maintained in NbSm1 medium. Between days 25 and 30, these chunks were harvested with Accutase (Sigma-Aldrich, no. A6964) and passaged onto PDL/laminin–coated culture dishes for the final experiments. Neuralization factors were freshly added from days 1 to 40 to 50, after which the neurons were kept in NbSm1 medium. The identification of dopaminergic lineage neurons was achieved through immunocytochemical staining for DA, midbrain, and neuronal markers at day 30 of differentiation. Only fully mature midbrain dopaminergic neurons at day 70 of differentiation were used for experimental analysis.

EB formation

Human iPSC colonies were rendered as a single-cell suspension by using Accutase (Sigma-Aldrich, no. A6964). Cells were centrifuged (300*g* × 4 min), resuspended, and seeded into a 96-well ultralow-attachment spheroid microplate (Corning, no. 4520) in E6 medium at a density of 1.5×10^4 cells per well. Immediately after seeding the cells, the plates were briefly centrifuged (100*g* × 3 min) to allow them to evenly spread at the bottom of the wells. On day 7, formed EBs were plated onto PDL/laminin–coated plates in KO DMEM F12 medium (Thermo Fisher Scientific) supplemented with 10% heat-inactivated fetal bovine serum (inactivation performed at 56° for 30 min). After additional 7 days of spontaneous differentiation, attached EBs were harvested, and quantitative reverse transcription polymerase chain reaction analysis was performed for markers of the three germ layers.

RNA extraction and quantitative reverse transcription polymerase chain reaction

qPCR was performed as previously described (*90*). Briefly, total RNA was extracted and isolated using the RNeasy Mini Kit (Qiagen) following the vendor's protocol, and the RNA concentration was assessed using a NanoDrop 2000C (Thermo Fisher Scientific). cDNA was synthesized with 500 ng of RNA following the vendor's protocol (iScript cDNA Synthesis Kit Bio-Rad). SYBR green qPCR was conducted using the Fast SYBR Green Master Mix (Applied Biosystems) following the standard protocol and ran in triplicate on the StepOnePlus Real-Time PCR System (Applied Biosystems). Data were quantified using the ΔCt (change in cycle threshold) method and normalized to glyceraldehyde-3-phosphate dehydrogenase (GAPDH) as a reference gene (Table 1).

Reprogramming of MEFs to iPSCs

MEFs were received from *DJ-1* KO and WT mice described earlier (*91*). MEFs were reprogrammed into iPSCs using the CytoTune-iPS 2.0 Sendai reprogramming kit (Thermo Fisher Scientific, no. A16518) following the vendor's standardized protocol. iPSCs generated from MEFs derived from three WT mice were expanded, and one clone per animal was used for experiments. iPSCs generated from MEFs derived from one DJ-1 KO mouse were expanded, and two clones of these iPSC lines were used for experiments.

Mouse iPSC culture and neural differentiation

Mouse iPSCs were cultured as a floating sphere on low-attachment plates located in an incubator provided with a constant shaking

Table 1. Primer details. Sequences for forward/reverse primer pairs for characterization of EB formation and pluripotency markers and housekeeping genes.

	Target	Primer (5′-3′)
Embryoid body formation	NCAM-F	ATGGAAACTCTATTAAAGTGAACCTG
	NCAM-R	TAGACCTCATACTCAGCATTCCAGT
	PAX6-F	GTCCATCTTTGCTTGGGAAA
	PAX6-R	TAGCCAGGTTGCGAAGAACT
	AFP-F	AGCTTGGTGGTGGATGAAAC
	AFP-R	CCCTCTTCAGCAAAGCAGAC
	SOX17-F	CTCTGCCTCCTCCACGAA
	SOX17-R	CAGAATCCAGACCTGCACAA
	MHY6-F	TCAGCTGGAGGCCAAAGTAAAGGA
	MHY6-R	TTCTTGAGCTCTGAGCACTCGTCT
	MSX1-F	CGAGAGGACCCCGTGGATGCAGAG
	MSX1-R	GGCGGCCATCTTCAGCTTCTCCAG
Pluripotency markers	SOX2-F	GGG AAA TGG GAG GGG TGC AAA AGA GG
	SOX2-R	TTG CGT GAG TGT GGA TGG GAT TGG TG
	OCT3/4-F	AC AGG GGG AGG GGA GGA GCT AGG
	OCT3/4-R	CTT CCC TCC AAC CAG TTG CCC CAA AC
	Rex1-F	CAG ATC CTA AAC AGC TCG CAG AAT
	Rex1-R	GCG TAC GCA AAT TAA AGT CCA GA
	NANOG-F	CAG CCC CGA TTC TTC CAC CAG TCC C
	NANOG-R	CGG AAG ATT CCC AGT CGG GTT CAC C
	TERT-F	CCT GCT CAA GCT GAC TCG ACA CCG TG
	TERT-R	GGA AAA GCT GGC CCT GGG GTG GAG C
Housekeeping gene	GAPDH-F	TGCACCACCAACTGCTTAGC
	GAPDH-R	GGCATGGACTGTGGTCATGAG

plate. iPSCs were cultured in iPSC media (Knockout DMEM F12, 10% KnockOut Serum Replacement, 1% L-glutamine, 1% PenStrep, 1% MEM Non-Essential Amino Acids, and 55 μM β-mercaptoethanol) supplemented with ESGRO 2i-LIF (Millipore, no. ESG1121, 1:1000). Media were changed daily, and cells were passaged every 3 to 4 days as single cells.

Mouse neuronal differentiation was performed following published protocols (*92*) with some modifications. Briefly, iPSCs ready for passage were rendered into a single-cell suspension using TrypLE (Thermo Fisher Scientific). iPSCs (1×10^6 to 1.5×10^6) were seeded onto low-attachment, 10-cm dishes in iPSC media without ESGRO 2i-LIF and positioned in an incubator provided with a constant shaking plate for 3 days to form EBs. On day 4, EBs were gently collected and seeded onto 10-cm dishes coated with PDL/laminin in iPSC media without ESGRO 2i-LIF. The following day, once EBs were attached to the plate, media were changed to differentiation media [DMEM F-12, 1% N2 supplement, 1% PenStrep, 1% L-glutamine, and laminin (1 μg/ml)] supplemented with basic fibroblast growth factor 2 (10 ng/ml; R&D, no. 100-18b), fibroblast growth factor 8b (100 ng/ml; R&D, no. 423-F8-025/CF), and 10 nM SAG 1.3 (Sigma-Aldrich, no. 566660). Four days later, EBs were dissociated into single cells using TrypLE and seeded onto PDL/laminin–coated plates. After 2 days, basic fibroblast growth factor 2, fibroblast growth factor 8, and SAG 1.3 were removed from the media, and 200 μM ascorbic acid (Sigma-Aldrich, no. A5960) was added. After 6 days, media were further supplemented with brain-derived neurotrophic factor (10 ng/ml; R&D, no. 248-BDB-250/CF) and glial cell line–derived neurotrophic factor (10 ng/ml; R&D, no. 212-GD-01M), and cells were maintained until they were fully differentiated (30 days of differentiation).

Sample preparation for LC-MS/MS

A modified procedure for single-pot solid-phase enhanced sample preparation (SP3) was used (*93*). In short, 15 μg of protein lysate was mixed with $MgCl_2$ to a final concentration of 10 mM. After adding 25 U benzonase (Sigma-Aldrich), samples were incubated for 30 min at 37°C. Proteins were reduced and alkylated by adding dithiothreitol (Biozol) to a final concentration of 10 mM and then incubated for 30 min at 37°C. Iodoacetamide (Sigma-Aldrich) was then added to a final concentration of 40 mM, and the reaction was quenched by adding another portion of dithiothreitol. Proteins were then bound to 40 μg of a 1:1 mixture of hydrophilic and hydrophobic magnetic Sera-Mag SpeedBeads (Cytiva) with a final concentration of 80% ethanol (Sigma-Aldrich) for 30 min at room temperature. Two hundred microliters of 80% ethanol was used to wash the beads four times using a Dynamag-2 magnetic rack (Thermo Fisher Scientific). A total of 190 ng of LysC and 190 ng of trypsin (Promega) were added to 40 μl of 50 mM ammonium bicarbonate (ABC) for proteolytic digestion, and the mixture was then incubated for 16 hours at room temperature. The supernatants were dried by vacuum centrifugation after being filtered using 0.22-μm spin-filters (Costar Spin-X, Corning). Twenty microliters of 0.1% formic acid was used to dissolve the dehydrated peptides. The Qubit protein assay (Thermo Fisher Scientific) was used to quantify the peptide content following proteolytic processing.

LC-MS/MS analysis

LC-MS/MS proteomic analyses were conducted on a nanoElute system (Bruker Daltonics) that was online coupled with a timsTOF Pro mass spectrometer (Bruker Daltonics) equipped with a column oven. Three-hundred fifty nanograms of peptides was separated on a 15-cm (75-μm inside diameter) column self-packed with ReproSil-Pur 120 C18-AQ resin (1.9 μm, Dr. Maisch GmbH) using a 90-min binary gradient of water and acetonitrile supplemented with 0.1% formic acid at a flow rate of 300 nl/min and a column temperature of 50°C.

Data-independent acquisition parallel accumulation serial fragmentation was used. For peptide fragment ion spectra, 34 consecutive data-independent acquisition windows with a width of 26 mass/charge ratio (m/z) were placed after one MS1 complete scan. These windows overlapped by 1 m/z, spanning a scan range of 350 to 1200 m/z. Each ramp had two windows examined, and the ramp time was set at 100 ms. This resulted in a total cycle time of 1.9 s.

Data analysis of LC-MS/MS results

Label-free quantitation (LFQ) of proteins was carried out using DIA-NN (version 1.8) (*94*). A library-free search was conducted against a database of common contaminants from MaxQuant (246 entries) and one canonical protein per gene reference sequence database of humans that was downloaded from UniProt (download date: 01 March 2023; 20603 entries). Trypsin was classified as a protease, and two missed cleavages were permitted. Carbamidomethylation of cysteines was classified as a permanent modification, while oxidation of methionines and acetylation of protein N termini were classified as variable modifications. For the identification of proteins and peptides, a 1% false discovery rate (FDR) threshold was used.

The program Perseus (version 2.1.3.0) (*95*) was used to analyze the output. For protein LFQ, two identified peptides were necessary. For statistical testing, the protein LFQ intensities had to be $\log_2$ converted and have at least three valid values per experimental group. Student's t test was conducted to compare protein abundance changes between the two experimental groups on the basis of $\log_2$ LFQ intensity. Differentially expressed proteins were defined by a P value <0.05 and a protein $\log_2$ fold change larger than 0.5 or smaller than −0.5 for both *DJ-1* KO lines, respectively.

GO analysis was performed using the web-based program DAVID version 6.8 (*96*, *97*). Gene lists for either up- or down-regulated proteins were compared to all proteins detected in LC-MS/MS in all cell lines. Using an EASE score of 0.05, otherwise the default parameters, functional annotation charts were generated for molecular functions (GOTERM_MF_DIRECT), biological processes (GOTERM_BP_DIRECT), and cellular components (GOTERM_CC_DIRECT).

Blue-native polyacrylamide gel electrophoresis/MS (BN-PAGE/MS)

BN-PAGE was performed largely according to the manufacturer's instructions, and unless noted, BN-PAGE reagents were obtained from Invitrogen. Snap-frozen cell pellets from control and *DJ-1* KO dopaminergic neurons were resuspended and lysed in cold BN-PAGE lysis buffer [50 mM tris and 1% (w/v) digitonin, pH 7.40, freshly supplemented with protease and phosphatase inhibitor cocktail (PPhI), Sigma-Aldrich, PPC1010, 100×], incubated for 30 min on ice, and then spun at maximum speed in a tabletop centrifuge (15 min). The total protein concentration in the lysate supernatants was quantified via bicinchoninic acid assay (BC Assay protein quantitation kit, Interchim), and the lysate was aliquoted in single-use aliquots and snap-frozen in liquid nitrogen. On the day of use, the lysate aliquots were supplemented with NativePAGE Sample Buffer (4×) and NativePAGE 5% G-250 Sample Additive (to 0.25%), spun in a tabletop centrifuge to remove aggregates, and loaded on a 4 to 16% NativePAGE Bis-Tris Gel. The gel was run at 4°C at 150 V (60 min) and then at 250 V (90 min), and when performing Western blotting, the cathode buffer was switched from dark blue (0.02% Coomassie G-250) to light blue (0.002% Coomassie G-250) when the sample dye front reached about one-third of the gel length. For blotting, BN-PAGE transfer buffer (25 mM bicine, 25 mM bis-tris, and 1 mM EDTA) was used as a buffer system, and the gel was transferred on 0.45-μm polyvinylidene difluoride membranes (Immobilon-P, Sigma-Aldrich) at 4°C (25 V, 90 to 120 min). After blotting, the membrane was fixed in 8% acetic acid (15 min), washed extensively with methanol, then dried, and rehydrated in tris-buffered saline with Tween 20. From this point on, Western blotting followed the SDS-PAGE Western blotting protocol, with chemiluminescence detection.

For MS, protein complexes from control and *DJ-1* KO neurons were separated by BN-PAGE and, after the native electrophoresis, marker lanes and lysates were visualized with Coomassie blue stain, and the bands of interest were excised using sterile scalpels. The bands were then chopped in smaller pieces and transferred onto a 96-well plate. Gel pieces were washed with 50 mM ABC/50% ethanol buffer, followed by dehydration with absolute ethanol, reduction of proteins with 10 mM dithiothreitol in 50 mM ABC at 56°C for 45 min, and alkylation of proteins with 55 mM iodoacetamide in 50 mM ABC at room temperature for 30 min. Gel pieces were once again washed and dehydrated (twice for 15 min) as above, followed by overnight trypsin digestion [trypsin (12 ng/μl) in 50 mM ABC and 40 μl of trypsin solution per well] at 37°C. Peptides were stepwise extracted from gel pieces with 30% acetonitrile/3% trifluoroacetic acid (TFA), 70% acetonitrile, and 100% acetonitrile. Combined supernatants were dried down, mixed 1:1 with 5% acetonitrile/1% trifluoroacetic acid, and loaded on preconditioned custom-made stage tips (2× C18 disks). Stage tips were washed with 0.1% formic acid, and peptides were eluted with 80% acetonitrile/0.1% formic acid. Peptide mixtures were separated using an Easy-nLC1200 liquid chromatograph (Thermo Fisher Scientific), followed by analysis on a Q Exactive HF mass spectrometer (Thermo Fisher Scientific). MS data were processed with MaxQuant (version 2.6.7.0) and analyzed with Perseus (version 2.1.3.0). Matches to common contaminants, reversed identifications, and identifications relying solely on site-specific modifications were excluded before further analysis. After $\log_2$ transformation of LFQ intensities, proteins were filtered to include only those detected in at least three of four replicates in at least one group (control and *DJ-1* KO). Two-sample Student's t test was performed, comparing control versus *DJ-1* KO to identify significantly changed proteins.

Immunoprecipitation/MS (IP/MS)

For the IPs, snap-frozen dopaminergic neuron pellets were resuspended and lysed in cold IP lysis buffer [50 mM tris, 150 mM NaCl, 1% NP-40, 0.15% (w/v) bovine serum albumin (BSA), 10% (w/v) glycerol, and 100× PPhI, pH 8.00], incubated for 30 min on ice, and then spun at maximum speed in a tabletop centrifuge (15 min). Pooled lysate supernatants of three six-well plate wells were used as the input for each IP reaction and diluted to 1 ml in IP wash buffer (10 mM tris, 140 mM NaCl, 0.1% *n*-octyl-β-D-glucopyranoside, 5 mM EDTA, and 100× PPhI, pH 8.00). Five micrograms of anti–PARK7/DJ1 antibody (EP2815Y, Abcam) was then added to each tube, and the IP reactions were rotated overnight at 4°C. On the next day, using wide-bore tips, 40 μl (80 μl of slurry) of Pierce Protein A Agarose beads (Thermo Fisher Scientific) was added to each reaction, and the tubes were rotated for two more hours at 4°C. The beads were then spun in a cooled tabletop centrifuge (2500*g*, 5 min) and, after the removal of the immunodepleted supernatant, washed with IP wash buffer. Beads were washed 4× with IP wash buffer and 2× with 50 mM ABC buffer, pH 8.00; then dried; snap-frozen in liquid nitrogen; and stored at −80°C. On-bead digestion and MS were performed as previously described (*98*).

Immunofluorescence staining and image analysis

Immunocytochemistry was performed using an adapted version of a previously published protocol (*90*). Cells were fixed in 4% paraformaldehyde (PFA) for 15 min, washed three times in phosphate-buffered saline (PBS), and then permeabilized for 30 min with 0.3% Triton X-100. Following permeabilization, coverslips were blocked with 0.3% Triton X-100 in 5% normal goat serum and 1% BSA in PBS for 1 hour. Coverslips were incubated overnight with the respective primary antibody against SOX2 (Abcam, no. AB79351; 1:100), Nanog (Abcam, no. AB80892; 1:100), OCT4 (Abcam, no. AB19857; 1:100), SSEA4 (Merck, MAB4304; 1:100), TuJ (β-III-tubulin) (BioLegend, no. 801201; 1:100; BioLegend, no. 802001; 1:100), LMX1a (Abcam, no. ab10533; 1:100), FOXA2 (Santa Cruz, no. sc-101060; 1:100), and TH (Merck, no. A657012; 1:100). The day after, coverslips were washed three times with PBS and incubated for 1 hour at room temperature with the respective secondary antibodies against anti-mouse or anti-rabbit Alexa Fluor 488 or 568 (Invitrogen, no. A11034; 1:1000; Invitrogen, no. A11031; 1:1000). The secondary antibody was washed three times with PBS, and coverslips were incubated with DAPI (4′,6-diamidino-2-phenylindole) for 5 min. Coverslips were then washed three times in PBS and once in sterile H_2O before being mounted on ProLong mounting media (Thermo Fisher Scientific).

For mouse iPSCs, spheres were collected at the moment of passage, centrifuged at 150*g* × 2 min, resuspended, and fixed in 4% PFA for 30 min with gentle shaking. After fixation, spheres were washed 3× in PBS (centrifugation-resuspension) and then permeabilized with 0.3% Triton X-100 for 30 min with gentle shaking. After permeabilization, spheres were blocked with 0.3% Triton X-100 in 5% normal goat serum and 1% BSA (1:1 ratio) in PBS for 1 hour with gentle shaking. Spheres were then incubated with gentle shaking overnight with the respective primary antibody against SOX2 (no. AB79351 at 1:100), Nanog (Abcam, no. AB80892 at 1:100), OCT4 (Abcam, no. AB19857 at 1:100), SSEA1 (Merck, MAB4301; 1:100). The day after, the spheres were washed three times with PBS and incubated for 1 hour at room temperature with the respective secondary antibody against anti-mouse or anti-rabbit Alexa Fluor 488 or 568 (Invitrogen, no. A11034; 1:1000; Invitrogen, no. A11031; 1:1000). Spheres were washed three times with PBS and incubated with DAPI for 5 min at room temperature with gentle shaking. Spheres were then washed three times in PBS and once in sterile H_2O before being placed as drops on glass microscope glasses. Microscope glasses were quickly placed on a heated thermo block until water evaporated, and then a glass coverslip was mounted using the ProLong mounting media (Thermo Fisher Scientific).

Images were captured using a confocal microscope (Leica Stellaris 5, Leica Microsystems, Wetzlar, Germany) provided with a dry 20× objective or an oil immersion 40× and 63× objective. For each coverslip, at least three fields of view were examined.

Labeling of neurons for confocal and MINFLUX-DNA PAINT imaging

iPSC-derived midbrain dopaminergic neurons from both *DJ-1* KO and their CRISPR-edited control lines were grown on 24-mm coverslips. Before labeling, the neurons were fixed at day 70 of differentiation using 4% PFA for 15 min, and the coverslips were washed twice, permeabilized for 5 min (0.3% Triton X-100; Thermo Fisher Scientific, A16046-AE), blocked with 5% normal goat serum for 1 hour, and incubated with primary antibodies for VMAT2 (Abcam, no. ab259970), VGLUT (SySy, no. 135408), VGAT (SySy, no. 131008), and Piccolo (Synaptic Systems, no. 142104) overnight. The next day, for confocal imaging, primary antibodies were removed, washed twice, and incubated with dye-labeled secondary antibodies (Abcam, nos. ab150079 and ab150185) for 1 hour. Afterward, the coverslips were washed thrice, and the samples were imaged under confocal microscopy within 1 day. For MINFLUX imaging, after primary antibody incubation, the neurons were washed and incubated with nanobodies coupled to a specific single-stranded DNA docking strand (Massive Photonics, MASSIVE-SDAB2-PLEX) for 1 hour at room temperature. Last, the samples were washed thrice and postfixed using PFA, followed by a washing step using PBS.

MINFLUX imaging

Before imaging, each coverslip was incubated with fiducial gold beads (150 nm; BBI Solutions, EM.GC20/7) for 5 to 10 min, and the nonimmobilized beads were removed by washing with PBS. The fiducial beads ensured the nanometer-scale stability of the sample during measurements by an active stabilization system that detected the 3D positions of the beads by a separated beamline and coupled with a galvanometer for real-time drift correction. Next, single-stranded DNA imager strands that are complimentary to the docking strands (Massive Photonics) were added to the sample and transferred to the microscope. Initially, the neurons were imaged in confocal mode, and individual synapses were identified using the punctate Piccolo signal, which were chosen as specific regions of interest (ROIs) (<2.25-μm^2 area). Each ROI was assigned at least eight neighboring gold beads as fiducial markers, and for every ROI, MINFLUX imaging was performed for 1 hour. Overall, the bead drift during the entire imaging duration was negligible with an average standard error of less than 1 nm.

The optical setup contained three different illumination modalities provided through separate optical paths: (i) wide-field excitation (488, 560, and 640 nm), (ii) regularly focused excitation (560 or 642 nm) or focused activation (405 nm), and (iii) phase-modulated excitation (560 or 642 nm), leading to a 3D donut in the focal region. The scanning range of all beams was about 100 μm by 100 μm in the lateral direction and 800 nm in the axial direction. A 1.4–numerical aperture oil immersion lens focused the excitation light into the sample and collected the fluorescence light. In contrast to the acquisition of fluorophore blinking events in regular SMLM, the transient binding of the imager strand with the docking strand acted as the blinking event. Imspector from Abberior Instruments was used as the microscopy acquisition software, and images were rendered using Paraview software.

MINFLUX image analysis

MINFLUX data were analyzed using a custom code written in Python. In MINFLUX, each "track" (tid) represents multiple detections (localizations) from single putative fluorophores. First, to filter spurious or background signals, we removed the tracks that contained less than four localizations. Next, to detect whether each track corresponds to single fluorophores, a cluster analysis was performed using the Gaussian mixture model on localizations that belonged to the same track to split distinct clusters, and a new list of tracks (tid2) was created. The localizations that belonged to each tid2 were combined into "events," which provided the localization precision [Fig. 3C, standard error of the mean (SEM)] of single fluorophores. Furthermore, another cluster analysis of the "events" was performed using DBSCAN for a range of epsilon values (10 to 100 nm) and minimum points, MinPts (1 to 3). The results were examined for the size and distribution of clusters, allowing the selection of appropriate epsilon value for specific proteins. For VMAT2, an epsilon of 40 nm and MinPt 3 rendered a homogeneous population of clusters with an average diameter of ~47 nm, which is in the expected range for synaptic vesicles. The abnormally large-sized vesicles (>100 nm in diameter), although detected with the same settings, were not included in the average size determination for the vesicles but were separately compared between the *DJ-1* KO and control neurons (Fig. 5C).

Protein extraction and Western blot analysis

Cultured neurons were collected by scraping in chilled PBS and centrifuged at 500*g* for 5 min. Cell pellets were successively homogenized using a lysis buffer containing 1% Triton X-100 (with 10% glycerol, 150 mM NaCl, 25 mM Hepes at pH 7.4, 1 mM EDTA, 1.5 mM $MgCl_2$, and a proteinase inhibitor cocktail). The protein solution was quantified using a bicinchoninic acid assay, and 10 μg was subjected to SDS-PAGE on gradient gels under reducing conditions. The gels were transferred onto polyvinylidene difluoride membranes and blocked with a Licor Intercept blocking solution. The primary antibodies used for Western blotting included the following: anti-GAPDH (1:10,000; Millipore, no. MAB374; 1:10,000; Cell Signaling, no. 2118), anti–tubulin β-3 (1:10,000; BioLegend, nos. 802001 and 801201), anti–Tyrosine hydroxylase (1:1000; Millipore, no. AB152), anti–PARK7/DJ1 (1:5000; Abcam, no. ab76008), anti–α-synuclein (syn303; BioLegend, no. 824301; 1:200; C-20; Santa Cruz, no. sc-7011-R; 1:1000), anti-Clathrin Heavy Chain (A-8) (Santa Cruz, no. sc-271178; 1:100), and anti-VMAT2 (Abcam, no. ab191121; 1:500). The blots were subsequently probed with the corresponding fluorescent secondary antibody (IRDye, Li-Cor) and visualized using the Odyssey Fc Imaging System (Li-Cor). For horseradish peroxidase–based blots, membranes were instead probed with a secondary horseradish peroxidase–coupled antibody (TrueBlot, Rockland), followed by revelation with the Clarity Max Western ECL substrate (Bio-Rad), and visualized using the Odyssey Fc Imaging System (Li-Cor).

False fluorescent neurotransmitter assay

FFN206 (Abcam, no. ab144554) was used in accordance with the published in vitro assays (*36*). On days 25 to 30 of differentiation, 100,000 cells per well were seeded into 96-well plates (Falcon 96-well Black/Clear Flat Bottom TC-treated Imaging Microplate) in preparation for live-cell staining. After that, the plates were cultured until day 90 of differentiation. After adding 100 μl per well of 1 μM FFN206 diluted in culture medium, the whole plate was incubated for 1 hour at 37°C. The VMAT2 inhibitor tetrabenazine (Sigma-Aldrich, no. T2952) functions as the negative control of the assay. Neurons were treated with 10 μM tetrabenazine for 30 min before adding FFN206. Photometric analysis of fluorescence uptake was carried out using excitation/emission wavelengths of 360 to 20/460 to 30 nm after one wash with PBS. Results were normalized to the total protein concentration.

Assessment of mitochondrial membrane potential using TMRE

To perform live-cell staining, 96-well plates (Falcon 96-well Black/Clear Flat Bottom TC-treated Imaging Microplate) were seeded with 100,000 cells per well on days 25 to 30. The plates were then kept in culture until day 90. Unless otherwise noted, staining methods were carried out according to the manufacturer's instructions. Two drops per milliliter of Hoechst 33342 (Invitrogen, no. R37605) were used to stain the cell nuclei after TMRE (Abcam, no. ab113852) had been diluted to 200 nM. After preparing dilutions in culture medium, 100 μl per well was added, and the mixture was incubated for 30 min. Following two PBS or 0.2% BSA washes, photometric analysis was performed using excitation/emission wavelengths of 360 to 20/460 to 30 nm (Hoechst 33342) and 540 to 15/584 to 20 nm (TMRE).

ATP assay

For ATP detection, the ATP Colorimetric/Fluorometric Assay Kit (Sigma-Aldrich, no. MAK190) was used. Freshly harvested cells were lysed in 100 μl of ATP assay buffer and deproteinized using a cellulose 10-kDa molecular weight cutoff spin filter (Sigma-Aldrich, no. UFC501008). Two to fifty microliters of samples was added into duplicate wells of a 96-well plate and subsequently brought to a final volume of 50 μl by adding ATP assay buffer. Reaction mixes were set up according to the schemes in the ATP assay protocol from Sigma-Aldrich, and 50 μl was added to each of the wells. By gently pipetting up and down, thorough mixing of components in each well was ensured, followed by a 30-min incubation in the dark at room temperature to protect the plate from light during incubation. ATP standards for fluorometric detection were prepared as described in the kit protocol. The fluorescent signal was measured by a BMG Labtech CLARIOstar Plus microplate reader using excitation/emission wavelengths of 535/587 nm.

ATP treatment (including the ATP-γ-S nonactive form)

For the ATP treatment of dopaminergic neurons, 50 μM of either ATP (Sigma-Aldrich, no. A6419) or its nonactive form ATP-γ-S (Bio-Log, no. A060), or the carrier H_2O was applied to neurons of a patient with DJ-1–linked PD and *DJ-1* KO neurons for 72 hours before harvesting and refreshing the treatment and media every 24 hours.

Transmission EM

iPSC-derived midbrain dopaminergic neurons were seeded onto plasma-treated ACLAR (plastic) films (Science Services). We treated cells with prewarmed 2× fixative [5% glutaraldehyde (EM-grade, Science Services) and 0.2 M cacodylate buffer, pH 7.4 (Science Services)] 1:1 to the culture medium. After 5 min, this mixture was replaced with 1× fixative (2.5% glutaraldehyde in 0.1 M cacodylate buffer) and incubated for 25 min on ice. Postfixation and postcontrasting were performed by several washes in 0.1 M cacodylate buffer on ice followed by incubation in 1% osmium tetroxide (Science Services) and 0.8% potassium ferrocyanide (Sigma-Aldrich) in 0.1 M sodium cacodylate buffer. Neuronal cells were further contrasted using 0.5% uranyl acetate in water (Science Services). After dehydration in ethanol and infiltration in LX112 resin (Ladd Research), the cell monolayer was embedded into resin blocks and cured for 48 hours at 60°C. Ultrathin sections (80 nm thick) were generated on a Leica UC6 ultramicrotome and adhered to formvar-coated copper grids (Plano). The sections were imaged on a JEM 1400plus (JEOL) transmission electron microscope using a XF416 camera (TVIPS) and the EM-Menu software (TVIPS). Image analysis was conducted using Fiji (*99*).

nIRF detection of oxidized DA

nIRF assay for the detection of oxidized DA was performed as previously described in detail (*3, 40*). Briefly, after being scraped in cold PBS, neurons were centrifuged for 5 min at 500*g*. Triton X-100 lysis buffer (1%) containing 10% glycerol, 150 mM NaCl, 25 mM Hepes, pH 7.4, 1 mM EDTA, 1.5 mM $MgCl_2$, and proteinase inhibitor cocktail was used to homogenize the cell pellet. Boiling and sonication were performed to recover insoluble pellets from a 100,000*g* spin (30 min, 4°C) in 2% SDS/50 mM tris, pH 7.4, which were then incubated for 30 min at 4°C. After a 150,000*g* spin, leftover pellets were further extracted in 1 mol/L NaOH and incubated overnight at 55°C. Depending on the solubility of the remaining sample, the solution was either vortexed or sonicated to guarantee total solubilization. A lyophilization step using a Speed Vac Concentrator was done to lyophilize the fluid until a dried pellet remained. To remove the remaining hydroxides and to lower pH levels, the pellet was first washed in Nanopure water. It was then lyophilized again until it was fully dry and then taken up in Nanopure water for final analysis. A stock of 10 mM oxidized DA was used to create the standard. To prepare oxidized DA, 10 mM DA and 20 mM $NaIO_4$ were combined in Dulbecco's PBS, vortexed, and then incubated for 5 min at room temperature. The solution was subsequently processed using centrifugation, sonication, and lyophilization techniques, the same as the neuron samples. An Odyssey infrared imaging system (Li-Cor) with the 700 channel was used to scan the membranes after 5 μl of each sample or standard dilution was dropped onto a Biodyne Nylon Transfer Membrane (Pall, no. Pall-60209). Odyssey infrared imaging software was used to quantify the samples.

Statistical analysis

Unpaired Student's *t* test was conducted for statistics in Figs. 3 (A, D, F, and G), 4 (A and B), and 5C and fig. S7 (E and F). An analysis of variance (ANOVA) followed by Šidák's multiple comparisons tests was conducted for statistics in Figs. 4 (D to F), 5D, 6 (A and B), and 7 (A to E) and fig. S6A.

For Fig. 1 (A and C) and figs. S3B and S4B, raw MS data were processed using DIA-NN (v1.8), whereas for Fig. 2C and fig. S5A, raw MS data were processed using MaxQuant (version 2.6.7.0). Statistical analysis was performed with Perseus (version 2.1.3.0). Differences between groups were assessed using two-sample Student's *t* test. Proteins were considered significantly differentially expressed if they had an FDR < 0.05 [$-\log_{10}(P) > 1.3$] and a $\log_2$ fold change >1.

P values <0.05 were considered significant, and all error bars in the figures represent the SEM ($*P < 0.05$; $**P < 0.01$; $***P < 0.001$). CTRL #1 and #2 values are combined as "CTRLs," and *DJ-1* KO #1 and #2 values are combined as "*DJ-1*$^{\mathrm{KOs}}$." A minimum of three differentiations were used for statistical analysis.

Supplementary Materials

The PDF file includes:
Figs. S1 to S7
Uncropped immunoblots
Legends for tables S1 to S3

Other Supplementary Material for this manuscript includes the following:
Tables S1 to S3

REFERENCES

1. V. Pitz, M. B. Makarious, S. Bandres-Ciga, H. Iwaki, 23andMe Research Team, A. B. Singleton, M. Nalls, K. Heilbron, C. Blauwendraat, Analysis of rare Parkinson's disease variants in millions of people. *NPJ Parkinsons Dis.* **10**, 11 (2024).
2. D. J. Surmeier, J. A. Obeso, G. M. Halliday, Selective neuronal vulnerability in Parkinson disease. *Nat. Rev. Neurosci.* **18**, 101–113 (2017).
3. L. F. Burbulla, P. Song, J. R. Mazzulli, E. Zampese, Y. C. Wong, S. Jeon, D. P. Santos, J. Blanz, C. D. Obermaier, C. Strojny, J. N. Savas, E. Kiskinis, X. Zhuang, R. Kruger, D. J. Surmeier, D. Krainc, Dopamine oxidation mediates mitochondrial and lysosomal dysfunction in Parkinson's disease. *Science* **357**, 1255–1261 (2017).
4. D. Sulzer, J. Bogulavsky, K. E. Larsen, G. Behr, E. Karatekin, M. H. Kleinman, N. Turro, D. Krantz, R. H. Edwards, L. A. Greene, L. Zecca, Neuromelanin biosynthesis is driven by excess cytosolic catecholamines not accumulated by synaptic vesicles. *Proc. Natl. Acad. Sci. U.S.A.* **97**, 11869–11874 (2000).
5. J. Meiser, D. Weindl, K. Hiller, Complexity of dopamine metabolism. *Cell Commun. Signal* **11**, 34 (2013).
6. T. G. Hastings, M. J. Zigmond, Loss of dopaminergic neurons in parkinsonism: Possible role of reactive dopamine metabolites. *J. Neural Transm. Suppl.* **49**, 103–110 (1997).
7. D. Sulzer, L. Zecca, Intraneuronal dopamine-quinone synthesis: A review. *Neurotox. Res.* **1**, 181–195 (2000).
8. M. J. LaVoie, B. L. Ostaszewski, A. Weihofen, M. G. Schlossmacher, D. J. Selkoe, Dopamine covalently modifies and functionally inactivates parkin. *Nat. Med.* **11**, 1214–1221 (2005).
9. D. M. Kuhn, R. E. Arthur Jr., D. M. Thomas, L. A. Elferink, Tyrosine hydroxylase is inactivated by catechol-quinones and converted to a redox-cycling quinoprotein: Possible relevance to Parkinson's disease. *J. Neurochem.* **73**, 1309–1317 (1999).
10. F. A. Zucca, J. Segura-Aguilar, E. Ferrari, P. Munoz, I. Paris, D. Sulzer, T. Sarna, L. Casella, L. Zecca, Interactions of iron, dopamine and neuromelanin pathways in brain aging and Parkinson's disease. *Prog. Neurobiol.* **155**, 96–119 (2017).
11. F. A. Zucca, E. Basso, F. A. Cupaioli, E. Ferrari, D. Sulzer, L. Casella, L. Zecca, Neuromelanin of the human substantia nigra: An update. *Neurotox. Res.* **25**, 13–23 (2014).
12. L. Zecca, F. A. Zucca, H. Wilms, D. Sulzer, Neuromelanin of the substantia nigra: A neuronal black hole with protective and toxic characteristics. *Trends Neurosci.* **26**, 578–580 (2003).
13. J. N. Guzman, J. Sanchez-Padilla, D. Wokosin, J. Kondapalli, E. Ilijic, P. T. Schumacker, D. J. Surmeier, Oxidant stress evoked by pacemaking in dopaminergic neurons is attenuated by DJ-1. *Nature* **468**, 696–700 (2010).
14. J. D. Erickson, L. E. Eiden, Functional identification and molecular cloning of a human brain vesicle monoamine transporter. *J. Neurochem.* **61**, 2314–2317 (1993).
15. E. N. Pothos, K. E. Larsen, D. E. Krantz, Y. Liu, J. W. Haycock, W. Setlik, M. D. Gershon, R. H. Edwards, D. Sulzer, Synaptic vesicle transporter expression regulates vesicle phenotype and quantal size. *J. Neurosci.* **20**, 7297–7306 (2000).
16. D. M. Omiatek, A. J. Bressler, A. S. Cans, A. M. Andrews, M. L. Heien, A. G. Ewing, The real catecholamine content of secretory vesicles in the CNS revealed by electrochemical cytometry. *Sci. Rep.* **3**, 1447 (2013).
17. C. Pifl, A. Rajput, H. Reither, J. Blesa, C. Cavada, J. A. Obeso, A. H. Rajput, O. Hornykiewicz, Is Parkinson's disease a vesicular dopamine storage disorder? Evidence from a study in isolated synaptic vesicles of human and nonhuman primate striatum. *J. Neurosci.* **34**, 8210–8218 (2014).
18. S. Ishikawa, Y. Tanaka, K. Takahashi-Niki, T. Niki, H. Ariga, S. M. Iguchi-Ariga, Stimulation of vesicular monoamine transporter 2 activity by DJ-1 in SH-SY5Y cells. *Biochem. Biophys. Res. Commun.* **421**, 813–818 (2012).
19. Y. Lu, W. Chen, C. Wei, Y. Zhu, R. Xu, Potential common genetic risks of sporadic Parkinson's disease and amyotrophic lateral sclerosis in the han population of mainland China. *Front. Neurosci.* **15**, 753870 (2021).
20. S. H. Lim, S. K. Kwon, M. K. Lee, J. Moon, D. G. Jeong, E. Park, S. J. Kim, B. C. Park, S. C. Lee, S. E. Ryu, D. Y. Yu, B. H. Chung, E. Kim, P. K. Myung, J. R. Lee, Synapse formation regulated by protein tyrosine phosphatase receptor T through interaction with cell adhesion molecules and Fyn. *EMBO J.* **28**, 3564–3578 (2009).
21. M. Toth, S. Alhabib, B. Manoury, R. Bobe, V. Leblais, SERCA3, ubiquitous but specific calcium pumps? *Cell Calcium* **132**, 103079 (2025).
22. K. A. Stout, A. R. Dunn, C. Hoffman, G. W. Miller, The synaptic vesicle glycoprotein 2: Structure, function, and disease relevance. *ACS Chem. Nerosci.* **10**, 3927–3938 (2019).

23. C. Patzke, M. M. Brockmann, J. Dai, K. J. Gan, M. K. Grauel, P. Fenske, Y. Liu, C. Acuna, C. Rosenmund, T. C. Sudhof, Neuromodulator signaling bidirectionally controls vesicle numbers in human synapses. *Cell* **179**, 498–513.e22 (2019).
24. T. W. Rosahl, D. Spillane, M. Missler, J. Herz, D. K. Selig, J. R. Wolff, R. E. Hammer, R. C. Malenka, T. C. Sudhof, Essential functions of synapsins I and II in synaptic vesicle regulation. *Nature* **375**, 488–493 (1995).
25. T. C. Sudhof, The presynaptic active zone. *Neuron* **75**, 11–25 (2012).
26. A. F. R. Batista, J. C. Martinez, U. Hengst, Intra-axonal synthesis of SNAP25 is required for the formation of presynaptic terminals. *Cell Rep.* **20**, 3085–3098 (2017).
27. G. Fischer von Mollard, B. Stahl, A. Khokhlatchev, T. C. Sudhof, R. Jahn, Rab3C is a synaptic vesicle protein that dissociates from synaptic vesicles after stimulation of exocytosis. *J. Biol. Chem.* **269**, 10971–10974 (1994).
28. J. Watson, M. Smith, C. Francavilla, J. M. Schwartz, SubcellulaRVis: A web-based tool to simplify and visualise subcellular compartment enrichment. *Nucleic Acids Res.* **50**, W718–W725 (2022).
29. D. Szklarczyk, R. Kirsch, M. Koutrouli, K. Nastou, F. Mehryary, R. Hachilif, A. L. Gable, T. Fang, N. T. Doncheva, S. Pyysalo, P. Bork, L. J. Jensen, C. von Mering, The STRING database in 2023: Protein-protein association networks and functional enrichment analyses for any sequenced genome of interest. *Nucleic Acids Res.* **51**, D638–D646 (2023).
30. J. O. Wirth, L. Scheiderer, T. Engelhardt, J. Engelhardt, J. Matthias, S. W. Hell, MINFLUX dissects the unimpeded walking of kinesin-1. *Science* **379**, 1004–1010 (2023).
31. K. C. Gwosch, J. K. Pape, F. Balzarotti, P. Hoess, J. Ellenberg, J. Ries, S. W. Hell, MINFLUX nanoscopy delivers 3D multicolor nanometer resolution in cells. *Nat. Methods* **17**, 217–224 (2020).
32. I. Boussaad, C. D. Obermaier, Z. Hanss, D. R. Bobbili, S. Bolognin, E. Glaab, K. Wolynska, N. Weisschuh, L. De Conti, C. May, F. Giesert, D. Grossmann, A. Lambert, S. Kirchen, M. Biryukov, L. F. Burbulla, F. Massart, J. Bohler, G. Cruciani, B. Schmid, A. Kurz-Drexler, P. May, S. Duga, C. Klein, J. C. Schwamborn, K. Marcus, D. Woitalla, D. M. Vogt Weisenhorn, W. Wurst, M. Baralle, D. Krainc, T. Gasser, B. Wissinger, R. Kruger, A patient-based model of RNA mis-splicing uncovers treatment targets in Parkinson's disease. *Sci. Transl. Med.* **12**, eaau3960 (2020).
33. R. D. Blakely, R. H. Edwards, Vesicular and plasma membrane transporters for neurotransmitters. *Cold Spring Harb. Perspect. Biol.* **4**, a005595 (2012).
34. T. S. Guillot, G. W. Miller, Protective actions of the vesicular monoamine transporter 2 (VMAT2) in monoaminergic neurons. *Mol. Neurobiol.* **39**, 149–170 (2009).
35. A. I. Bernstein, K. A. Stout, G. W. Miller, A fluorescent-based assay for live cell, spatially resolved assessment of vesicular monoamine transporter 2-mediated neurotransmitter transport. *J. Neurosci. Methods* **209**, 357–366 (2012).
36. G. Hu, A. Henke, R. J. Karpowicz Jr., M. S. Sonders, F. Farrimond, R. Edwards, D. Sulzer, D. Sames, New fluorescent substrate enables quantitative and high-throughput examination of vesicular monoamine transporter 2 (VMAT2). *ACS Chem. Biol.* **8**, 1947–1954 (2013).
37. J. I. Aguilar, M. Dunn, S. Mingote, C. S. Karam, Z. J. Farino, M. S. Sonders, S. J. Choi, A. Grygoruk, Y. Zhang, C. Cela, B. J. Choi, J. Flores, R. J. Freyberg, B. D. McCabe, E. V. Mosharov, D. E. Krantz, J. A. Javitch, D. Sulzer, D. Sames, S. Rayport, Z. Freyberg, Neuronal depolarization drives increased dopamine synaptic vesicle loading via VGLUT. *Neuron* **95**, 1074–1088.e7 (2017).
38. V. N. Murthy, P. De Camilli, Cell biology of the presynaptic terminal. *Annu. Rev. Neurosci.* **26**, 701–728 (2003).
39. M. Kaksonen, A. Roux, Mechanisms of clathrin-mediated endocytosis. *Nat. Rev. Mol. Cell Biol.* **19**, 313–326 (2018).
40. J. R. Mazzulli, L. F. Burbulla, D. Krainc, H. Ischiropoulos, Detection of free and protein-bound ortho-quinones by near-infrared fluorescence. *Anal. Chem.* **88**, 2399–2405 (2016).
41. J. R. Mazzulli, A. J. Mishizen, B. I. Giasson, D. R. Lynch, S. A. Thomas, A. Nakashima, T. Nagatsu, A. Ota, H. Ischiropoulos, Cytosolic catechols inhibit alpha-synuclein aggregation and facilitate the formation of intracellular soluble oligomeric intermediates. *J. Neurosci.* **26**, 10068–10078 (2006).
42. J. R. Mazzulli, M. Armakola, M. Dumoulin, I. Parastatidis, H. Ischiropoulos, Cellular oligomerization of alpha-synuclein is determined by the interaction of oxidized catechols with a C-terminal sequence. *J. Biol. Chem.* **282**, 31621–31630 (2007).
43. D. E. Mor, E. Tsika, J. R. Mazzulli, N. S. Gould, H. Kim, M. J. Daniels, S. Doshi, P. Gupta, J. L. Grossman, V. X. Tan, R. G. Kalb, K. A. Caldwell, G. A. Caldwell, J. H. Wolfe, H. Ischiropoulos, Dopamine induces soluble α-synuclein oligomers and nigrostriatal degeneration. *Nat. Neurosci.* **20**, 1560–1568 (2017).
44. R. Taipa, C. Pereira, I. Reis, I. Alonso, A. Bastos-Lima, M. Melo-Pires, M. Magalhaes, DJ-1 linked parkinsonism (PARK7) is associated with Lewy body pathology. *Brain* **139**, 1680–1687 (2016).
45. K. Solti, W. L. Kuan, B. Forizs, G. Kustos, J. Mihaly, Z. Varga, B. Herberth, E. Moravcsik, R. Kiss, M. Karpati, A. Mikes, Y. Zhao, T. Imre, J. C. Rochet, F. Aigbirhio, C. H. Williams-Gray, R. A. Barker, G. Toth, DJ-1 can form β-sheet structured aggregates that co-localize with pathological amyloid deposits. *Neurobiol. Dis.* **134**, 104629 (2020).
46. Y. Liu, X. Ma, H. Fujioka, J. Liu, S. Chen, X. Zhu, DJ-1 regulates the integrity and function of ER-mitochondria association through interaction with IP3R3-Grp75-VDAC1. *Proc. Natl. Acad. Sci. U.S.A.* **116**, 25322–25328 (2019).
47. L. Y. Hao, B. I. Giasson, N. M. Bonini, DJ-1 is critical for mitochondrial function and rescues PINK1 loss of function. *Proc. Natl. Acad. Sci. U.S.A.* **107**, 9747–9752 (2010).
48. G. Krebiehl, S. Ruckerbauer, L. F. Burbulla, N. Kieper, B. Maurer, J. Waak, H. Wolburg, Z. Gizatullina, F. N. Gellerich, D. Woitalla, O. Riess, P. J. Kahle, T. Proikas-Cezanne, R. Kruger, Reduced basal autophagy and impaired mitochondrial dynamics due to loss of Parkinson's disease-associated protein DJ-1. *PLOS ONE* **5**, e9367 (2010).
49. X. Wang, T. G. Petrie, Y. Liu, J. Liu, H. Fujioka, X. Zhu, Parkinson's disease-associated DJ-1 mutations impair mitochondrial dynamics and cause mitochondrial dysfunction. *J. Neurochem.* **121**, 830–839 (2012).
50. X. Wang, Y. Li, Y. Qian, Y. Cao, P. Shriwas, H. Zhang, X. Chen, Extracellular ATP, as an energy and phosphorylating molecule, induces different types of drug resistances in cancer cells through ATP internalization and intracellular ATP level increase. *Oncotarget* **8**, 87860–87877 (2017).
51. G. M. Forte, E. Davie, S. Lie, M. Franz-Wachtel, A. J. Ovens, T. Wang, J. S. Oakhill, B. Macek, I. M. Hagan, J. Petersen, Import of extracellular ATP in yeast and man modulates AMPK and TORC1 signalling. *J. Cell Sci.* **132**, jcs223925 (2019).
52. I. H. Chaudry, Does ATP cross the cell plasma membrane. *Yale J. Biol. Med.* **55**, 1–10 (1982).
53. M. T. Henrich, W. H. Oertel, D. J. Surmeier, F. F. Geibl, Mitochondrial dysfunction in Parkinson's disease—A key disease hallmark with therapeutic potential. *Mol. Neurodegener.* **18**, 83 (2023).
54. M. L. Bucher, C. W. Barrett, C. J. Moon, A. D. Mortimer, E. A. Burton, J. T. Greenamyre, T. G. Hastings, Acquired dysregulation of dopamine homeostasis reproduces features of Parkinson's disease. *NPJ Parkinsons Dis.* **6**, 34 (2020).
55. K. M. Lohr, A. I. Bernstein, K. A. Stout, A. R. Dunn, C. R. Lazo, S. P. Alter, M. Wang, Y. Li, X. Fan, E. J. Hess, H. Yi, L. M. Vecchio, D. S. Goldstein, T. S. Guillot, A. Salahpour, G. W. Miller, Increased vesicular monoamine transporter enhances dopamine release and opposes Parkinson disease-related neurodegeneration in vivo. *Proc. Natl. Acad. Sci. U.S.A.* **111**, 9977–9982 (2014).
56. I. T. Hsiao, Y. H. Weng, C. J. Hsieh, W. Y. Lin, S. P. Wey, M. P. Kung, T. C. Yen, C. S. Lu, K. J. Lin, Correlation of Parkinson disease severity and 18F-DTBZ positron emission tomography. *JAMA Neurol.* **71**, 758–766 (2014).
57. C. L. Liang, O. Nelson, U. Yazdani, P. Pasbakhsh, D. C. German, Inverse relationship between the contents of neuromelanin pigment and the vesicular monoamine transporter-2: Human midbrain dopamine neurons. *J. Comp. Neurol.* **473**, 97–106 (2004).
58. C. E. Glatt, A. D. Wahner, D. J. White, A. Ruiz-Linares, B. Ritz, Gain-of-function haplotypes in the vesicular monoamine transporter promoter are protective for Parkinson disease in women. *Hum. Mol. Genet.* **15**, 299–305 (2006).
59. D. S. Goldstein, P. Sullivan, C. Holmes, G. W. Miller, S. Alter, R. Strong, D. C. Mash, I. J. Kopin, Y. Sharabi, Determinants of buildup of the toxic dopamine metabolite DOPAL in Parkinson's disease. *J. Neurochem.* **126**, 591–603 (2013).
60. N. Takahashi, L. L. Miner, I. Sora, H. Ujike, R. S. Revay, V. Kostic, V. Jackson-Lewis, S. Przedborski, G. R. Uhl, VMAT2 knockout mice: Heterozygotes display reduced amphetamine-conditioned reward, enhanced amphetamine locomotion, and enhanced MPTP toxicity. *Proc. Natl. Acad. Sci. U.S.A.* **94**, 9938–9943 (1997).
61. E. Isingrini, C. Guinaudie, C. P. L. Q. Rainer, L. Moquin, A. Gratton, B. Giros, Genetic elimination of dopamine vesicular stocks in the nigrostriatal pathway replicates Parkinson's disease motor symptoms without neuronal degeneration in adult mice. *Sci. Rep.* **7**, 12432 (2017).
62. W. M. Caudle, J. R. Richardson, M. Z. Wang, T. N. Taylor, T. S. Guillot, A. L. McCormack, R. E. Colebrooke, D. A. Di Monte, P. C. Emson, G. W. Miller, Reduced vesicular storage of dopamine causes progressive nigrostriatal neurodegeneration. *J. Neurosci.* **27**, 8138–8148 (2007).
63. N. Lev, Y. Barhum, N. S. Pilosof, D. Ickowicz, H. Y. Cohen, E. Melamed, D. Offen, DJ-1 protects against dopamine toxicity: Implications for Parkinson's disease and aging. *J. Gerontol. A Biol. Sci. Med. Sci.* **68**, 215–225 (2013).
64. M. Gonzalez-Sepulveda, J. Compte, T. Cuadros, A. Nicolau, C. Guillard-Sirieix, N. Penuelas, M. Lorente-Picon, A. Parent, J. Romero-Gimenez, J. M. Cladera-Sastre, A. Laguna, M. Vila, In vivo reduction of age-dependent neuromelanin accumulation mitigates features of Parkinson's disease. *Brain* **146**, 1040–1052 (2023).
65. A. Laguna, N. Penuelas, M. Gonzalez-Sepulveda, A. Nicolau, S. Arthaud, C. Guillard-Sirieix, M. Lorente-Picon, J. Compte, L. Miquel-Rio, H. Xicoy, J. Liu, A. Parent, T. Cuadros, J. Romero-Gimenez, G. Pujol, L. Gimenez-Llort, P. Fort, A. Bortolozzi, I. Carballo-Carbajal, M. Vila, Modelling human neuronal catecholaminergic pigmentation in rodents recapitulates age-related neurodegenerative deficits. *Nat. Commun.* **15**, 8819 (2024).
66. R. H. Kim, P. D. Smith, H. Aleyasin, S. Hayley, M. P. Mount, S. Pownall, A. Wakeham, A. J. You-Ten, S. K. Kalia, P. Horne, D. Westaway, A. M. Lozano, H. Anisman, D. S. Park, T. W. Mak, Hypersensitivity of DJ-1-deficient mice to 1-methyl-4-phenyl-1,2,3,6-tetrahydropyridine (MPTP) and oxidative stress. *Proc. Natl. Acad. Sci. U.S.A.* **102**, 5215–5220 (2005).

67. M. S. Goldberg, A. Pisani, M. Haburcak, T. A. Vortherms, T. Kitada, C. Costa, Y. Tong, G. Martella, A. Tscherter, A. Martins, G. Bernardi, B. L. Roth, E. N. Pothos, P. Calabresi, J. Shen, Nigrostriatal dopaminergic deficits and hypokinesia caused by inactivation of the familial Parkinsonism-linked gene DJ-1. *Neuron* **45**, 489–496 (2005).
68. L. Chen, B. Cagniard, T. Mathews, S. Jones, H. C. Koh, Y. Ding, P. M. Carvey, Z. Ling, U. J. Kang, X. Zhuang, Age-dependent motor deficits and dopaminergic dysfunction in DJ-1 null mice. *J. Biol. Chem.* **280**, 21418–21426 (2005).
69. J. van der Beek, C. de Heus, N. Liv, J. Klumperman, Quantitative correlative microscopy reveals the ultrastructural distribution of endogenous endosomal proteins. *J. Cell Biol.* **221**, e202106044 (2022).
70. Y. C. Wong, D. Krainc, α-Synuclein toxicity in neurodegeneration: Mechanism and therapeutic strategies. *Nat. Med.* **23**, 1–13 (2017).
71. L. Stefanis, α-Synuclein in Parkinson's disease. *Cold Spring Harb. Perspect. Med.* **2**, a009399 (2012).
72. A. L. Mahul-Mellier, J. Burtscher, N. Maharjan, L. Weerens, M. Croisier, F. Kuttler, M. Leleu, G. W. Knott, H. A. Lashuel, The process of Lewy body formation, rather than simply α-synuclein fibrillization, is one of the major drivers of neurodegeneration. *Proc. Natl. Acad. Sci. U.S.A.* **117**, 4971–4982 (2020).
73. S. Shendelman, A. Jonason, C. Martinat, T. Leete, A. Abeliovich, DJ-1 is a redox-dependent molecular chaperone that inhibits alpha-synuclein aggregate formation. *PLoS Biol.* **2**, e362 (2004).
74. R. Kumar, S. Kumar, P. Hanpude, A. K. Singh, T. Johari, S. Majumder, T. K. Maiti, Partially oxidized DJ-1 inhibits α-synuclein nucleation and remodels mature α-synuclein fibrils in vitro. *Commun. Biol.* **2**, 395 (2019).
75. C.-Y. Xu, W.-Y. Kang, Y.-M. Chen, T.-F. Jiang, J. Zhang, L.-N. Zhang, J.-Q. Ding, J. Liu, S.-D. Chen, DJ-1 inhibits α-synuclein aggregation by regulating chaperone-mediated autophagy. *Front. Aging Neurosci.* **9**, 308 (2017).
76. M. E. Larson, S. J. Greimel, F. Amar, M. LaCroix, G. Boyle, M. A. Sherman, H. Schley, C. Miel, J. A. Schneider, R. Kayed, F. Benfenati, M. K. Lee, D. A. Bennett, S. E. Lesne, Selective lowering of synapsins induced by oligomeric α-synuclein exacerbates memory deficits. *Proc. Natl. Acad. Sci. U.S.A.* **114**, E4648–E4657 (2017).
77. J. Choi, M. C. Sullards, J. A. Olzmann, H. D. Rees, S. T. Weintraub, D. E. Bostwick, M. Gearing, A. I. Levey, L. S. Chin, L. Li, Oxidative damage of DJ-1 is linked to sporadic Parkinson and Alzheimer diseases. *J. Biol. Chem.* **281**, 10816–10824 (2006).
78. O. A. Buneeva, A. E. Medvedev, DJ-1 protein and its role in the development of Parkinson's disease: Studies on experimental models. *Biochemistry (Mosc.)* **86**, 627–640 (2021).
79. A. H. Schapira, C. W. Olanow, J. T. Greenamyre, E. Bezard, Slowing of neurodegeneration in Parkinson's disease and Huntington's disease: Future therapeutic perspectives. *Lancet* **384**, 545–555 (2014).
80. A. Bose, M. F. Beal, Mitochondrial dysfunction in Parkinson's disease. *J. Neurochem.* **139**, 216–231 (2016).
81. L. M. Heger, R. M. Wise, J. T. Hees, A. B. Harbauer, L. F. Burbulla, Mitochondrial phenotypes in Parkinson's diseases—A focus on human iPSC-derived dopaminergic neurons. *Cells* **10**, 3436 (2021).
82. H. Watanabe, S. Shima, K. Kawabata, Y. Mizutani, A. Ueda, M. Ito, Brain network and energy imbalance in Parkinson's disease: Linking ATP reduction and α-synuclein pathology. *Front. Mol. Neurosci.* **17**, 1507033 (2025).
83. S. C. Cunnane, E. Trushina, C. Morland, A. Prigione, G. Casadesus, Z. B. Andrews, M. F. Beal, L. H. Bergersen, R. D. Brinton, S. de la Monte, A. Eckert, J. Harvey, R. Jeggo, J. H. Jhamandas, O. Kann, C. M. la Cour, W. F. Martin, G. Mithieux, P. I. Moreira, M. P. Murphy, K. A. Nave, T. Nuriel, S. H. R. Oliet, F. Saudou, M. P. Mattson, R. H. Swerdlow, M. J. Millan, Brain energy rescue: An emerging therapeutic concept for neurodegenerative disorders of ageing. *Nat. Rev. Drug Discov.* **19**, 609–633 (2020).
84. C. E. Toomey, W. E. Heywood, J. R. Evans, J. Lachica, S. N. Pressey, S. C. Foti, M. Al Shahrani, K. D'Sa, I. P. Hargreaves, S. Heales, M. Orford, C. Troakes, J. Attems, E. Gelpi, M. Palkovits, T. Lashley, S. M. Gentleman, T. Revesz, K. Mills, S. Gandhi, Mitochondrial dysfunction is a key pathological driver of early stage Parkinson's. *Acta Neuropathol. Commun.* **10**, 134 (2022).
85. J. Burrone, Z. Li, V. N. Murthy, Studying vesicle cycling in presynaptic terminals using the genetically encoded probe synaptopHluorin. *Nat. Protoc.* **1**, 2970–2978 (2006).
86. P. Seibler, J. Graziotto, H. Jeong, F. Simunovic, C. Klein, D. Krainc, Mitochondrial Parkin recruitment is impaired in neurons derived from mutant PINK1 induced pluripotent stem cells. *J. Neurosci.* **31**, 5970–5976 (2011).
87. J. R. Mazzulli, F. Zunke, O. Isacson, L. Studer, D. Krainc, α-Synuclein-induced lysosomal dysfunction occurs through disruptions in protein trafficking in human midbrain synucleinopathy models. *Proc. Natl. Acad. Sci. U.S.A.* **113**, 1931–1936 (2016).
88. L. F. Burbulla, S. Jeon, J. Zheng, P. Song, R. B. Silverman, D. Krainc, A modulator of wild-type glucocerebrosidase improves pathogenic phenotypes in dopaminergic neuronal models of Parkinson's disease. *Sci. Transl. Med.* **11**, eaau6870 (2019).
89. S. Kriks, J. W. Shim, J. Piao, Y. M. Ganat, D. R. Wakeman, Z. Xie, L. Carrillo-Reid, G. Auyeung, C. Antonacci, A. Buch, L. Yang, M. F. Beal, D. J. Surmeier, J. H. Kordower, V. Tabar, L. Studer, Dopamine neurons derived from human ES cells efficiently engraft in animal models of Parkinson's disease. *Nature* **480**, 547–551 (2011).
90. F. Gubinelli, L. Sarauskyte, C. Venuti, I. Kulacz, G. Cazzolla, M. Negrini, D. Anwer, I. Vecchio, F. Jakobs, F. P. Manfredsson, M. Davidsson, A. Heuer, Characterisation of functional deficits induced by AAV overexpression of alpha-synuclein in rats. *Curr. Res. Neurobiol.* **4**, 100065 (2023).
91. T. T. Pham, F. Giesert, A. Röthig, T. Floss, M. Kallnik, K. Weindl, S. M. Hölter, U. Ahting, H. Prokisch, L. Becker, T. Klopstock, M. H. de Angelis, K. Beyer, K. Görner, P. J. Kahle, D. M. V. Weisenhorn, W. Wurst, DJ-1-deficient mice show less TH-positive neurons in the ventral tegmental area and exhibit non-motoric behavioural impairments. *Genes Brain Behav.* **9**, 305–317 (2010).
92. T. Oosterveen, P. Garcao, E. Moles-Garcia, C. Soleilhavoup, M. Travaglio, S. Sheraz, R. Peltrini, K. Patrick, V. Labas, L. Combes-Soia, U. Marklund, P. Hohenstein, L. Panman, Pluripotent stem cell derived dopaminergic subpopulations model the selective neuron degeneration in Parkinson's disease. *Stem Cell Rep.* **16**, 2718–2735 (2021).
93. C. S. Hughes, S. Moggridge, T. Muller, P. H. Sorensen, G. B. Morin, J. Krijgsveld, Single-pot, solid-phase-enhanced sample preparation for proteomics experiments. *Nat. Protoc.* **14**, 68–85 (2019).
94. V. Demichev, C. B. Messner, S. I. Vernardis, K. S. Lilley, M. Ralser, DIA-NN: Neural networks and interference correction enable deep proteome coverage in high throughput. *Nat. Methods* **17**, 41–44 (2020).
95. S. Tyanova, J. Cox, Perseus: A bioinformatics platform for integrative analysis of proteomics data in cancer research. *Methods Mol. Biol.* **1711**, 133–148 (2018).
96. D. W. Huang, B. T. Sherman, R. A. Lempicki, Systematic and integrative analysis of large gene lists using DAVID bioinformatics resources. *Nat. Protoc.* **4**, 44–57 (2009).
97. B. T. Sherman, M. Hao, J. Qiu, X. Jiao, M. W. Baseler, H. C. Lane, T. Imamichi, W. Chang, DAVID: A web server for functional enrichment analysis and functional annotation of gene lists (2021 update). *Nucleic Acids Res.* **50**, W216–W221 (2022).
98. N. Y. Kochanova, T. Schauer, G. P. Mathias, A. Lukacs, A. Schmidt, A. Flatley, A. Schepers, A. W. Thomae, A. Imhof, A multi-layered structure of the interphase chromocenter revealed by proximity-based biotinylation. *Nucleic Acids Res.* **48**, 4161–4178 (2020).
99. J. Schindelin, I. Arganda-Carreras, E. Frise, V. Kaynig, M. Longair, T. Pietzsch, S. Preibisch, C. Rueden, S. Saalfeld, B. Schmid, J.-Y. Tinevez, D. J. White, V. Hartenstein, K. Eliceiri, P. Tomancak, A. Cardona, Fiji: An open-source platform for biological-image analysis. *Nat. Methods* **9**, 676–682 (2012).
100. Y. Perez-Riverol, C. Bandla, D. J. Kundu, S. Kamatchinathan, J. Bai, S. Hewapathirana, N. S. John, A. Prakash, M. Walzer, S. Wang, J. A. Vizcaino, The PRIDE database at 20 years: 2025 update. *Nucleic Acids Res.* **53**, D543–D553 (2025).

Acknowledgments: We thank R. Krüger for providing iPSC lines from a patient with DJ-1–linked PD and its CRISPR-edited control, P. Seibler for providing iPSC lines from two healthy control individuals, and D. Krainc for providing respective CRISPR-edited *DJ-1* KO lines. We thank C. Haass for providing equipment and assistance. We thank S. Langer-Freitag and I. Sikora at the Institute of Human Genetics, Klinikum Rechts der Isar, School of Medicine, Technical University of Munich, for karyotyping of mouse iPSC lines. We thank the Protein Analytics Unit at the Biomedical Center, Ludwig Maximilian University of Munich, and I. Forné for providing equipment, technical expertise, and assistance with data analysis. **Funding:** This work was supported by the European Research Council (ERC) under the European Union's Horizon 2020 research and innovation programme (grant agreement no. 948027) (to L.F.B.), by the Rise up! programme of the Boehringer Ingelheim Foundation (BIS) (to L.F.B.), by Deutsche Forschungsgemeinschaft (DFG; German Research Foundation) under the Heisenberg Programme (project no. 447395247) (to L.F.B.) and under Germany's Excellence Strategy within the framework of the Munich Cluster of Systems Neurology (EXC 2145 SyNergy—ID 390857198) (to L.F.B., M.S., S.F.L., and C.B.), and by Bundesministerium für Bildung und Forschung (BMBF; FKZ: 01ED2402A) under the aegis of JPND (to S.F.L.). The work of W.W. was supported by the Helmholtz Association "ExNet-0041-Phase2-3 ('SyNergy-HMGU')." M.R. thanks the Hector Fellow Academy for support. **Author contributions:** L.M.H.: writing—original draft, conceptualization, investigation, writing—review and editing, methodology, data curation, validation, formal analysis, and visualization. F.G.: writing—original draft, investigation, writing—review and editing, methodology, resources, validation, formal analysis, and visualization. A.J.H.: investigation, writing—review and editing, resources, validation, formal analysis, and visualization. A.C.-A.: writing—original draft, writing—review and editing, methodology, resources, data curation, software, and visualization. M.R.: investigation, writing—review and editing, formal analysis, and visualization. U.M.: investigation, writing—review and editing, and resources. S.A.M.: investigation, writing—review and editing, methodology, formal analysis, and visualization. S.R.N.: investigation and formal analysis. L.J.: investigation, writing—review and editing, methodology, validation, and formal analysis. M.S.: investigation and resources. W.W.: investigation, writing—review and editing, methodology, resources, funding acquisition, supervision, and project administration. S.F.L.: investigation, writing—review and editing, methodology, resources, funding acquisition, supervision, and project administration. C.B.: resources, funding acquisition, supervision, and formal analysis. S.S.: writing—original draft, investigation,

writing—review and editing, methodology, resources, data curation, validation, supervision, formal analysis, software, and visualization. L.F.B.: writing—original draft, conceptualization, investigation, writing—review and editing, methodology, resources, funding acquisition, validation, supervision, project administration, and visualization. **Competing interests:** The authors declare that they have no competing interests. **Data and materials availability:** All data and code needed to evaluate and reproduce the results in the paper are present in the paper and/or the Supplementary Materials. All MS/proteomic datasets reported in this study have been deposited to the ProteomeXchange Consortium via the PRIDE (*100*) partner repository and are publicly available via the accession number PXD069663 (www.ebi.ac.uk/pride/archive/projects/PXD069663), PXD069553 (www.ebi.ac.uk/pride/archive/projects/PXD069553), and PXD066098 (www.ebi.ac.uk/pride/archive/projects/PXD066098). The iPSC lines from a patient with DJ-1–linked PD and its CRISPR-edited control can be provided by R. Krüger pending scientific review and a completed material transfer agreement. Requests for these iPSC lines should be submitted to request.ncer-pd@uni.lu. The iPSC lines from two healthy control individuals and their CRISPR-edited DJ-1 KO counterparts can be provided by P. Seibler pending scientific review and a completed material transfer agreement. Requests for these iPSC lines should be submitted to philip.seibler@uni-luebeck.de. WT and DJ-1 KO MEFs for conversion to mouse iPSC lines can be provided by W. Wurst pending scientific review and a completed material transfer agreement. Requests for these MEFs should be submitted to wolfgang.wurst@helmholtz-munich.de.

Submitted 15 June 2025
Accepted 8 January 2026
Published 11 February 2026
10.1126/sciadv.adz5645

Science Advances

VMAT2 dysfunction impairs vesicular dopamine uptake, driving its oxidation and #-synuclein pathology in DJ-1–linked Parkinson's neurons

Leonie M. Heger, Francesco Gubinelli, Andreas J. Huber, Aida Cardona-Alberich, Matteo Rovere, Ulf Matti, Stephan A. Müller, Sankarshana R. Nagaraja, Lena Jaschkowitz, Martina Schifferer, Wolfgang Wurst, Stefan F. Lichtenthaler, Christian Behrends, Sivakumar Sambandan, and Lena F. Burbulla

Sci. Adv. **12** (7), eadz5645. DOI: 10.1126/sciadv.adz5645

Science Advances (ISSN 2375-2548) is published by the American Association for the Advancement of Science. 1200 New York Avenue NW, Washington, DC 20005. The title *Science Advances* is a registered trademark of AAAS.